Two dimensional simulations of VHF plasmas for industrial applications

蘇, 俐文

Two dimensional simulations of VHF plasmas for industrial applications

LiWen Su

Prof. Kiichiro Uchino

Ionized Gas Dynamics Laboratory

Department of Applied Science for Electronics and materials

Interdisciplinary Graduate School of Engineering Sciences

Kyushu University

March 2019

Contents

Abstract

This thesis deals with the topic of very high frequency (VHF) plasma simulations for industrial applications such as amorphous silicon thin film solar cells and the semiconductor fabrication. A VHF capacitively coupled plasma (CCP) source is widely used for plasma enhanced chemical vapor deposition (PECVD) and plasma etching. Industries require further cost reduction of solar cells and semiconductors. Larger area fabrication of films and fine etching are key technologies but they have been mostly carried out by trial and error. Recently, there is a trend of a large area and narrow gap discharge in industries, so it is limited to diagnose the VHF-CCP characteristics inside the vacuum chamber. Therefore, plasma simulation has become a powerful tool to accomplish the goals. This thesis consists of five chapters, and the last chapter 5 provides a summary of two dimensional simulations of VHF plasmas for industrial applications.

In this work, the VHF-CPPs of a frequency of 60 MHz in the PECVD process with multi-hollow geometry and multi-rod electrodes were examined, where the substrate was placed behind the discharge electrodes. Triode VHF-CCP sources using the multi-hollow

geometry and multi-rod electrodes were designed for achieving high deposition rate with high-quality films for amorphous silicon (a-Si) fabrication. As is well known, distribution of SiH_3 and SiH_2 radicals as well as the density and temperature of electrons are important parameters for deposition rates and higher-order silanes generation that is related to film quality of a-Si. In this thesis, it was focused to examine the VHF plasma characteristics and higher-order silanes generation using the plasma hybrid model, where 149 chemical reactions were considered.

In the first part, the multi-hollow geometry plasma was simulated for SiH_4/H_2 gas to prepare amorphous silicon. A typical character of the VHF plasma of a high electron density with a low electron temperature was obtained. The density ratio of SiH_3/SiH_2 that is a measure to judge film quality at the center and near the substrate was very large, indicating the fabrication of high-quality amorphous silicon. However, it was found that there were many higher-order silanes with high densities near the substrate. The density of Si_5H_{12} radicals that contribute to a dust formation was comparable to the SiH_3 density, suggesting generation of dust particles. Furthermore, the multi-hollow plasma effect was not found at the selected pressure.

In the following part of this thesis, the multi-rod electrode geometry was simulated for pure SiH_4 gas. It was found that the SiH_3 density was similar to that in the case of the multi-hollow plasma, however, high-order silanes densities near the substrate were

significantly lower than the SiH_3 density. Therefore, the multi-rod electrodes can fabricate high- quality films. To optimize the process of VHF plasma discharges in the multi-rod geometry, the simulations were performed at different pressures. Increases in pressure were found to negatively affect the deposition rate in the simulated geometry.

The last part of the thesis was dedicated to the simulation of a VHF argon plasma (100 MHz) at 5.3 Pa for etching process in a CCP geometry using the Particle In-Cell with Monte Carlo Collision Module. Plasma uniformity along the discharge electrodes is a key subject in plasma etching and has been studied using simulations by many researchers. In this study, two-dimensional PIC simulation was performed under the assumption that the plasma is produced by electrostatic fields. It was found that the electron density peaked near the edge of the discharge electrode and at the center, which is the first result found without taking into account electromagnetic fields. The results obtained by this simulation will be useful for designing a VHF plasma source for large-area etching processes.

Acknowledgements

I have written this thesis by the help of many.

Foremost, I would like to express my sincere appreciation to my supervisor Prof. Kiichiro Uchino, without his leading I couldn't finish my Ph.D research. I am also highly indebted to Prof. Yoshinobu Kawai, without his research idea and knowledge I couldn't have done that many simulation works.

Besides that, I would like to thank the rest of my thesis committee: Prof. Hiroshi Nakashima and Prof. Hayashi Nobuya, for their encouragement, insightful comments, and hard questions. It helps me to understand how the point of view of another field can enrich my own research and bring new ideas. How to explain properly to let the audiences and readers to understand.

I would like to thank Mitsubishi Corporation as well, to provide me with the scholarship for the last year of my Ph.D. With their scholarship I could focus on my research without any financial condition to worry about.

In the end, I would like to thank my friends and family for their never ceasing support and help.

Chapter 1

Introduction

1.1 General introduction

The concerns about environmental issues are growing together with the more frequent occurrence of irregular weather and potential ecological catastrophes. One of the recent topics is therefore switching to more environmentally friendly technologies for energy production. The current selection is very wide and spans from wind turbines to sea wave power generators. However, most of the effort during the last decades has been probably devoted to solar power applications such as solar photovoltaic (PV) power cells. The PV cells are currently going through a rapid development and they are increasing their installed area day by day. As an example can serve Taiwan, which is like Japan an island country with limited access to conventional sources of energy. The plan of Taiwan until 2030 is to increase the capacity of renewable energy sources to 9.95 GWe (peak) from the initial 3.5 GWe in 2009 [70, 72] mostly in form of offshore and onshore wind power and photovoltaic

panels. Similar situation can be observed in most of the developed countries in Europe, Asia and America as well [2, 14, 15, 22]. To achieve these goals massive government subsidies are offered and those funds are subsequently used for further research and development where major focus is in general on efficiency, production costs and endurance (i.e. degradation prevention). From the view of production costs the amorphous silicon has the most advantageous properties, however several issues concerning its conversion efficiency and endurance have been addressed. To solve these problems new ways of manufacturing are currently under development.

For manufacturing of the amorphous silicon thin film solar cells the thin film technology is needed. The traditional way to produce the thin film in industry is the Chemical Vapor Deposition (CVD) and for increasing the reaction rate of the precursors the Plasma Enhanced Chemical Vapor Deposition (PECVD) can be used. The principle of the CVD begins: First, the reactant gases are fed into the reactor chamber. The gases will spread inside of the chamber and some of the gases' volume start to interact with boundary wall immediately. The precursors atoms are adsorbed on the substrate's surface. The successfully adsorbed atoms migrate on the surface and interact with other atoms present on the surface of the substrate. Through the nucleation process the adsorbed atoms form nuclei then an island from which the film is grown. However, not all the atoms are used to create the film. These atoms which are not part of the surface reactions can desorb from the surface and became precursors of the volatile byproducts. Based on the CVD principle the

PECVD method is used to grow high quality film in a lower temperature manufacturing process.

A low temperature plasmas for industry applications consisting of electrons, ions, and active neutral species are generated by RF (Radio Frequency) discharges and often called reactive plasma. The purpose is to create a non-equilibrium state, that is, many chemical reactions different from those in equilibrium state can occur. Plasma technology has become increasingly important in solar cells and microelectronics manufacturing processes. Silane (SiH_4) gas is the basis of plasma technology for applications using silicon. Amorphous silicon is fabricated using a capacitively coupled SiH_4 plasma with a power source frequency of typically 13.56 MHz. The SiH_4 plasma is produced by electron impact ionizations and the chemical reactions are as follows:

$$\begin{aligned}
SiH_4 + e^- &\longrightarrow SiH_3{}^+ + H + 2\,e^- \\
SiH_4 + e^- &\longrightarrow SiH_2{}^+ + H_2 + 2\,e^- \\
SiH_4 + e^- &\longrightarrow SiH^+ + H_2 + H + 2\,e^- \\
SiH_4 + e^- &\longrightarrow Si^+ + 2\,H_2 + 2\,e^- \\
SiH_4 + e^- &\longrightarrow SiH_3{}^- + H \\
SiH_4 + e^- &\longrightarrow SiH_2{}^- + H_2
\end{aligned} \tag{1.1}$$

Above reactions indicate that positive ions (SiH^+, $SiH_2{}^+$ and $SiH_3{}^+$) and negative ions ($SiH_2{}^-$ and $SiH_3{}^-$) exist in the SiH_4 plasma. In fact, amorphous silicon had at-

tracted many solar cell researchers, however the deposition rate and conversion efficiency of amorphous silicon are low. Therefore, a lot of researches have been dedicated to these topics. Kroll et al. [30] fabricated amorphous silicon with a high deposition rate using a very high frequency (VHF) capacitively coupled plasma (CCP), and in addition, Shah et al. [60] proposed the tandem silicon thin film solar cell consisting of amorphous and microcrystalline silicon to increase the conversion efficiency of the solar cell.

Despite the success in fabrication method development, the cost reduction of silicon thin film solar cells has been the most important issue and many efforts to reduce the cost of silicon thin film solar cells have been made. However, the cost of the tandem silicon solar cell is still high compared with that of crystalline silicon solar cells. Therefore, amorphous silicon solar cells have considered once again [27, 42] because their manufacturing cost is much lower than that of the tandem silicon thin film solar cell. In addition, the structure of amorphous silicon solar cells is simple. On the other hand, there is a serious problem called "light induced degradation" [64], where the initial conversion efficiency of silicon thin film solar cells decreases after light soaking [40, 41, 48]. It is considered to be closely related to Si-H_2 bonds as well as higher-order silane radicals which play an important role in this light induced degradation [64]. Thus, the control of the light induced degradation has been an important subject in the development of amorphous/microcrystalline silicon solar cells. Matsuda et al. [40] tried to suppress this degradation and recently a hydrogen-dilution method, which is one of their suggestions, has been widely used to improve the

light-induced degradation. They also [41, 48] reported that, when H_2 gas was introduced into SiH_4 plasmas, the electron temperature increased and, as a result, additional reactions occurred and the ion bombardment energy increased. Thus, the electron temperature is an important parameter in the fabrication of amorphous silicon. Moreover, it is important in the development of silicon thin film solar cells to examine the characteristics of SiH_4 plasmas. Generally, the parameters of low-temperature plasmas are measured by the Langmuir probe method. However, the Langmuir probe method does not provide correct values in reactive plasmas such as SiH_4 plasmas because the probe is rapidly contaminated. In addition to the contamination, many chemical reactions occur in SiH_4 plasma and as a result, many positive ions (SiH_3^+, SiH_2^+, SiH^+, H^+, and so on) and negative ions (SiH_3^-, SiH_2^- and H^-) are generated that make the sheath complicated. So, it is difficult to estimate the parameters of the SiH_4 plasmas using a Langmuir probe. Therefore, the simulation will be a powerful tool for understanding the characteristics of SiH_4 plasmas.

To reduce the light-induced degradation, Matsuda et al. [40] also proposed the so-called triode plasma source, where the plasma generation region was separated from the film deposition region using a third negatively biased electrode (meshed electrode), and their group [61, 63] fabricated stable amorphous silicon films with a low Si-H_2 bond density using a 60 MHz VHF plasma. Takai et al. [66] reported that the contribution of higher order silanes to the film growth depends on the electron temperature, hydrogen dilution rate, gas flow rate, and gas temperature. Especially, it is interesting from the

point of view of plasma physics that low electron temperatures is required for reducing the higher order silanes contributions to the film growth. Recently, Matsui et al. [42] have fabricated amorphous silicon using a triode VHF-PECVD (frequency, 60 MHz), applied to the tandem solar cell, and achieved a stabilized conversion efficiency of 11.9%. However, the deposition rate was very low because of the use of the meshed electrode. In addition to a high-speed deposition, a large -area plasma ($> 1\ m^2$) has been required to reduce the cost of silicon thin film solar cells, so the meshed electrode will not be useful for actual PECVD. Thus, the development of a new triode plasma source that enables a high-speed deposition is required by solar cell industries.

There have been many reports on simulations of SiH_4 plasmas [31, 62]. As is well known, there are three kinds of simulation models to examine the behaviors of a low temperature plasma for applications, that is, fluid model, hybrid model, and particle-in-cell (PIC) model. The properties of SiH_4 plasmas have been extensively investigated using the fluid model by many researches. Kushner [31] proposed a perfect simulation model of SiH_4 plasmas using a one-dimensional hybrid code. The model dealt with the plasma chemistry of SiH_4 gas discharges. Used electron impact cross sections are presented in Appendix-1. As is well known, the main deposition precursor in SiH_4 plasmas is SiH_3 and the contribution of SiH_2 is much smaller than that of SiH_3, and SiH_2 affects the quality of the deposited films [31] and is called the precursor to form higher-order silanes. Main SiH_3 production processes in the SiH_4 plasmas are the electron collisional dissociation of

SiH_4 and hydrogen abstraction reaction [31], while most SiH_3 is lost by diffusion outside the discharge electrodes. In the case where high-quality amorphous silicon is prepared, the SiH_3 density is much higher than the SiH_2 and SiH densities [31, 48], such that the density ratio SiH_3/SiH_2 has been discussed as a measure of film quality. The neutral-neutral and polymerization reactions leading to the formation of higher-order radicals and molecules in SiH_4 plasmas were listed by Kushner [31], indicating that the following reaction plays an important role in the growth of amorphous silicon because SiH_3 radicals are removed by this reaction:

$$SiH_3 + SiH_3 \longrightarrow SiH_2 + SiH_4 \tag{1.2}$$

It has been found that there are three rate constants for the above reaction reported in the literature [31, 49, 57]. When studies of dust particles became popular, the rate constant proposed by Perrin et al. [57] was used in the simulations [12, 43]; Perrin et al.'s rate constant k_P ($= 1.5 \times 10^{-16}\,\mathrm{m^3\,s^{-1}}$) is two orders of magnitude higher than Kushner's rate constant k_K ($= 7 \times 10^{-18}\,\mathrm{m^3\,s^{-1}}$). NIST-PML [32] provides the middle value k_N ($= 3 \times 10^{-17}\,\mathrm{m^3\,s^{-1}}$).

As is well known, higher-order silanes are produced by successive insertion reactions of SiH_2 starting from $SiH_2 + SiH_4 \longrightarrow Si_2H_6$, $SiH_2 + Si_2H_6 \longrightarrow Si_3H_8$,..... to $SiH_2 + Si_{n-1}H_{2n} \longrightarrow Si_nH_{2n+2}$, leading to dust formation. In my thesis, silicon hydride molecules, Si_4H_{10} and Si_5H_{12}, and radicals, Si_4H_9 and Si_5H_{11}, were taken into account, where the NIST-PML's rate constant was used. To contribute to the development of the

triode plasma source that provides high deposition rates, a two-dimensional simulation of a triode VHF SiH_4 plasma was performed using the plasma hybrid code of the PEGASUS software [7, 8, 51, 53, 56]. To the best knowledge of the author, there is no report of the simulation of a triode VHF SiH_4 plasma using the rate constant of NIST-PML for reaction (1.2).

Plasma etching that is an indispensable technology for semiconductor fabrication is also one of applications of a VHF-CCP. Recently, industries have required high speed etching rates and controls of an electron energy distribution function (EEDF) and ion energy distribution function (IEDF). Thus, VHF plasma sources at excitation frequencies of 100-150 MHz have become popular in etching [13, 76]. As described, when the power source frequency is increased, the electron density increases, leading to a high etching rate. However, as is well known, electromagnetic effects such as standing wave and skin effects [33] arise at high frequencies, and as a result, the electron density distribution along the discharge electrodes becomes nonuniform [20]. In fact, Sawada et al. [59] observed that the electron density in the VHF Ar plasma at a frequency of 60 MHz had a center-peaked profile. Thus, the study of a spatial distribution of VHF Ar CCPs is an important subject in etching. In order to develop a new VHF CCP source for etching, the characteristics of VHF-Ar CCPs were studying using the PIC code of PEGASUS Software because the PIC simulation is useful at low pressures.

1.2 Outline of the thesis

The thesis is divided into five chapters as briefly summarized in the following: Chapter 1 is the introduction. Chapter 2 includes the explanations of very high frequency plasma, balanced power feeding method, two-dimensional plasma hybrid model, and Particle-in-cell (PIC) model. Chapter 3 describes two dimensional simulations of a triode VHF SiH_4 plasma (60 MHz) with the multi-hollow geometry and multi-rod electrodes using PEGASUS-PHM. Higher-order silanes such as Si_5H_{12} radicals are taken into account in the simulations. It was found that the multi-rod electrodes VHF discharge plasma can provide a high-quality silicon. Chapter 4 describes the characteristics of the VHF Ar plasma (100 MHz) using the PIC-MCCM of PEGASUS under the assumption that the plasma is produced by electrostatic fields. It was found that the plasma peaked near the edge of the discharge electrode and at the center. Finally, Chapter 5 includes conclusions and suggestions for future work.

Chapter 2

VHF-SiH_4 capacitively coupled plasma

2.1 VHF plasma

When electron and molecules collide, the chemical bond can be broken generating radicals and ions necessary for the deposition and etching processes. To increase the precursor reactivity in the reaction chamber, several parameters have to be considered. One of them is the ability to achieve high ionization rates which means to achieve a high electron density. Using a Very High Frequency (VHF) it is possible to achieve a high electron density and low electron temperature. The frequency of discharge should be smaller than the electron plasma frequency f_{pe} and much higher than the ion plasma frequency f_{pi}. In this way the electrons are trapped by the VHF potential of a frequency f_{VHF} between two parallel discharge electrodes while other particles are not effected as strongly inside the plasma and can move relatively freely.

$$f_{pi} \ll f_{VHF} < f_{pe} \tag{2.1}$$

For effective trapping the electron displacement δx should be shorter than the spacing gap d between discharge electrodes for $\omega \ll \nu_m$ [58],

$$\delta x = \frac{qE_0}{m_e \omega \nu_m} \ll \frac{d}{2} \tag{2.2}$$

where ω is the angular frequency of the VHF power source and ν_m is the electron-neutral collision frequency. q, m_e and E_0 are electron charge, electron mass and the amplitude of the VHF electric field, respectively.

The discharge frequency f_VHF cannot be changed beyond the validity of Eq. 2.1. That leaves the parameters E_0 and ν_m as the main variables to adjust the VHF plasma characteristics. Hence, to achieve higher electron trapping effect and high electron density the Eq. 2.2 declares to increase the pressure or the amplitude of the VHF electric field. To estimate the power P absorbed by the electrons the mean power density equation was used written in the following form

$$P = \frac{nq^2 E_0^2}{2m_e} \frac{\nu_m}{\nu_m^2 + \omega^2} \tag{2.3}$$

When $\nu_m \gg \omega$, P decreases in proportion to ν_m^{-1} , that is, the electron density decreases in inverse proportion to the pressure. Equations (2.2) and (2.3) suggest that the electron

density is considered to be maximum at a certain pressure although the electron density is determined by solving the particle and power balance equations. Recently, the above tendency has been found in simulations [52] as well as experiments [74]. Equation (2.2) indicates that E_0 is an important parameter for a VHF plasma. When the VHF power increases, the amplitude of an electron oscillation in the VHF electric field E_0 increases; as a result, the condition for electron trapping, $\delta x \ll \frac{d}{2}$, is not valid and the electrons reach the electrode before inverting of the electric field and are not trapped by the electrode. Therefore, to increase ν_m, by increasing pressure is required for the VHF discharge at high powers.

2.2 Balanced power feeding model

The usual way to apply the VHF power to the power electrode is via a coaxial cable, however, even with this kind of precautions it is problematic to avoid the VHF to leak in the vacuum chamber. To prevent the additional discharges and produce the plasma only between the electrodes, Nishimiya and his colleagues developed balance power feeding (BPF) method. In Appendix 2 is shown the schematic of the VHF power feeding method by (a) conventional method and by (b) new BPF method as presented in Nishimiya's work [47]. The point of the BPF is to use of a power divider which provides two output signals with 180 degrees phase shift from a single VHF power source. That BPF method itself is an experimental method with many factors to consider. For simplicity, an ideal case has been in general two separate power sources can be considered. In this simulation

environment, two VHF power sources were applied to realized the BPF method in an ideal application. An example is demonstrated by Eq. (2.11). Ogiwara et al. [51] applied the BPF method in the simulation of hydrogen plasma with high electron density and low electron temperature between the electrodes. The results of the Ogiwara's simulation showed that the BPF method can be effectively used to produce VHF plasma in the simulated environment. Here, Ogiwara's modeling was adopted.

2.3 Two-dimensional plasma hybrid model

Behaviors of low temperature plasma are generally described by the Boltzmann equation. When a device size is much larger than the mean free path of electrons and ions, groups of electrons and ions are regarded as a continuous medium, that is, the fluid equations derived from the Boltzmann equation are available for describing plasma behaviors [58, Chapter 5]. The fluid equations are described in Appendix 3. The Plasma Hybrid Module (PHM) of PEGASUS Software Inc. was used in this thesis. The PHM performs the simulations combining the Poisson's equation module (PEM), the electron Monte Carlo simulation module (EMCSM) and the drift-diffusion equation module (DDEM). The PEM calculates electric field with Poisson's equation by the semi-implicit method:

$$\nabla \cdot \varepsilon \nabla \phi \,(t + \Delta t) = \rho_{(t)} + \Delta t \frac{\partial \rho_{(t)}}{\partial t} + \rho_{(s)}(t + \Delta t) \tag{2.4}$$

Here, ε is the permittivity, ϕ is the electrostatic potential, and ρ is the electric charge density, respectively. ρ_s is the mean surface charge on the surface of dielectric and is taken into account in the cell next to dielectric. The electric field is obtained from the following equation:

$$E = -\nabla\phi \tag{2.5}$$

Electron energy distribution functions (EEDFs) are obtained by the EMCSM. The time-averaged EEDF $f(x, y, \varepsilon)$ is determined by a Monte Carlo simulation for temporal length of 1000 rf cycles with the electron density, which is calculated by the fluid model, and with the velocity and the position of the electrons, which are derived from the equation of electron motion. Here, x, y and ε are the horizontal position, vertical position and the electron energy, respectively. The electron temperature T_e is obtained from

$$T_e(r, z) = \frac{2}{3}\int_0^\infty \varepsilon\,(x, y)\, f\,(x, y, \varepsilon)\, d\varepsilon \tag{2.6}$$

The DDEM calculates the density and the velocity of ions by solving the equations of continuity in which the drift diffusion model is applied to the particle fluxes. The equation of continuity of ion species m is given by

$$\frac{\partial n_m}{\partial t} = -\nabla \cdot \Gamma_m + S_m \tag{2.7}$$

Here, n_m, Γ_m and S_m are the density, the flux and the source rate of the species m, respectively. S_m consists of coefficients of source and loss of the particles. The flux Γ_m is described as

$$\Gamma_m = \pm\mu_m n_m E - D_m \nabla n_m \tag{2.8}$$

where μ_m and D_m are the mobility and the diffusion coefficient of the species m. The temperatures of the ion species are fixed to the room temperature, so that the energy balance equations are not calculated here.

For neutral particles, the convection-diffusion equation and Navier-Stokes equation, which are described in the following, are derived,

$$\frac{\partial \rho_a}{\partial t} + \nabla \cdot \rho_a \mathbf{v} = -\nabla \cdot \mathbf{j_a} + S_a \tag{2.9}$$

$$\frac{\partial \rho \mathbf{v}}{\partial t} + \nabla \cdot \rho \mathbf{v}\mathbf{v} = -\nabla p + \nabla \cdot \mathbf{\Pi} + S_{mom} \tag{2.10}$$

Here, ρ_a j_a, and S_a Sa are mass density, diffusion flux, and source term of species a, respectively, and $\mathbf{v}, \rho, \mathbf{\Pi}$ p are velocity, mass density, viscous stress tensor and pressure of mixed gas, respectively. The value of S_{mom} is momentum transport through collision with the charged particles. In this model, the temperatures of ions and neutrals are fixed to a room temperature.

Input voltages V_t and V_b were applied to the top and the bottom electrodes:

$$V_t = V_{rf}cos(2\pi ft) + V_{dc,t}, V_b = V_{rf}cos(2\pi ft + \pi) + V_{dc,b} \tag{2.11}$$

where f and V_{rf} are the frequency and the amplitude of the VHF voltages, respectively. DC biases of each the electrode $V_{dc,t}$ and $V_{dc,b}$ vary self-consistently in the assumption that a blocking capacitor is connected to the electrodes. When the BPF is used, the self-bias voltage is 0 V, which has been confirmed by measuring it with an oscilloscope [51]. The input power applied to the electrodes P_{elec} is obtained by

$$P_{elec} = P_t + P_b = \frac{1}{T_{rf}} \int_0^{T_{rf}} (V_t I_t(t) + V_b I_b(t))\, dt \tag{2.12}$$

Here, V_{rf} is the time of a VHF cycle, and I_t and I_b are currents flow to the top and the bottom electrodes, respectively.

As reported by many researchers [31], key radicals in the SiH_4 plasma are SiH_3, SiH_2, SiH, Si and H, and they are mainly generated by the following electron impact dissociations:

$$\begin{aligned}
&\mathrm{SiH_4 + e^- \longrightarrow SiH_3 + H} \\
&\mathrm{SiH_4 + e^- \longrightarrow SiH_2 + H_2} \\
&\mathrm{SiH_4 + e^- \longrightarrow SiH + H_2 + H} \\
&\mathrm{SiH_4 + e^- \longrightarrow Si + 2\,H_2}
\end{aligned} \tag{2.13}$$

SiH_3 radicals are also produced by the so-called hydrogen abstraction $SiH_4 + H \longrightarrow SiH_3 + H_2$. Sticking coefficients S of SiH_3, SiH_2, and SiH radicals on the substrate and electrodes are important in silicon films growth. S is defined as $S = 1 - R$ where R is the reflection coefficient. In this simulation, it is assumed the sticking coefficients to be 0.1 for SiH_3, 0.8 for SiH_2, 0.8 for SiH, and 0.9 for Si [31]. In addition, those of higher-order silanes were assumed to be 1.0. The procedure of the simulation process using the PHM is illustrated in Fig. (2.1). In the simulations, more than 3,600,000 VHF periods cycles (1000 iterations with over 10,000 cycles each) are needed to achieve the convergence of the steady-state solution.

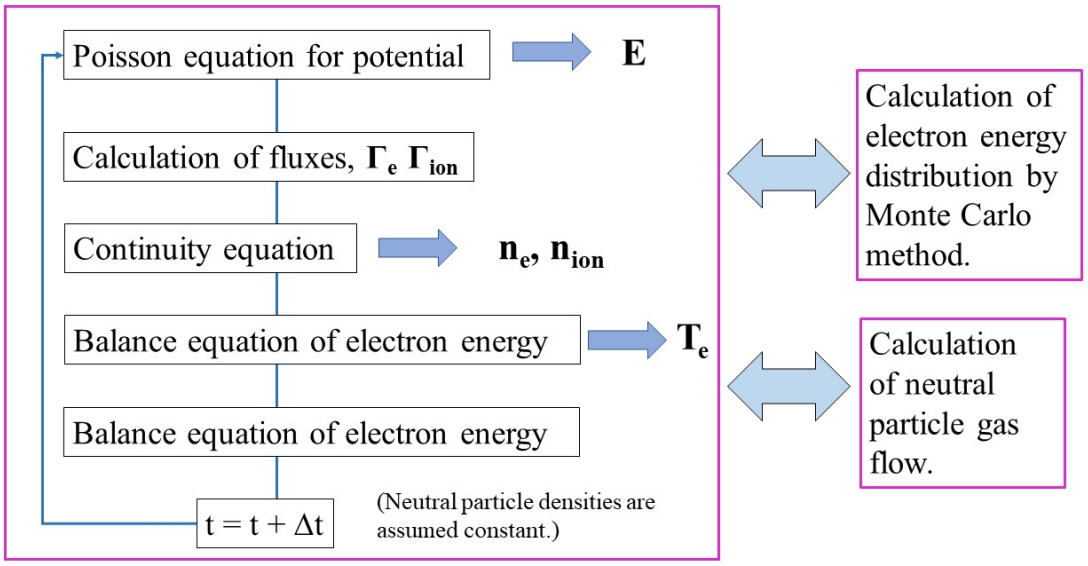

few back every few cycles.

Figure 2.1: Brief explanation of simulation procedure, where Γ_e and Γ_i are the flux of electrons and ions, and n_e and n_i are the electron and ion densities.

2.4 Two-dimensional PIC model

The particle-in-cell (PIC) method is based on a kinetic description of charged particle motions in phase space. Charged particles move in the self-consistent electric field that is obtained by solving the Poisson equation. The Monte Carlo method is used to calculate collisions including excitation and ionization. The PIC method has been described in detail by Birdsall [4], Turner [36], and Verboncoeur [37]. In the PIC method, electrons and ions are modeled as a large number of representative particles that are referred to as simulated particles (superparticles). A motion of the individual superparticle is subject to the Newton's law in the electric field. Various kinds of collisions are also taken into account using Monte Carlo collision module (MCCM). Macroscopic quantities of the electron and ion densities, mean energy, particle flux are obtained by statistical calculations using velocities and positions of all the superparticles. Here, PIC/MCCM of PEGASUS Software Inc. was used.

Chapter 3

Simulation results of SiH_4 plasma

3.1 Multi-hollow geometry plasma

3.1.1 Introduction

Recent research shows that a multi-hollow plasma source can provide a high electron density, leading to high deposition rates [24, 44, 45, 46]. Niikura et al. [44, 45, 46] investigated the multi-hollow cathode plasma source for microcrystalline silicon films with high rate growth at high pressures ranging from 400 to 1,300 Pa. In their work they have achieved flat-distributed stable high density-plasma spots on the cathode surface with the growth rate of $9.3\,\mathrm{nm\,s^{-1}}$ [44]. By achieving this they have prepared the foundation for large-area high-rate growth of μc-Si:H films by VHF-PECVD. In the following work the Niikura et al.[46] focused on limiting defect density. They have obtained a high deposition rate of $8\,\mathrm{nm\,s^{-1}}$ with the defect density of $5 \times 10^{15}\,\mathrm{cm^{-3}}$ demonstrating the effectiveness

of the multi-hollow cathode plasma source [45, 46]. Koga et al. [29] adopted the multi-hollow VHF plasma for fabrication of amorphous silicon, where a substrate was placed outside the discharge electrodes, that is, triode configuration, and obtained high quality films by introducing a cluster-eliminating filter [17]. In this case, however, the filter reduced the deposition rate. Thus, it is an important subject to look for optimum conditions for high quality amorphous silicon with high deposition rates. Therefore, in this work two dimensional simulations of a triode VHF SiH_4/H_2 plasma with a multi-hollow geometry was performed.

There have been many reports on simulations of SiH_4 plasmas relating to fabrication of amorphous silicon [3, 12, 24, 31, 43]. As is well known, the main deposition precursor in SiH_4 plasmas is SiH_3 and the contribution of SiH_2 is much smaller than that of SiH_3, and SiH_2 that is chemically reactive affects the quality of deposited films, that is, SiH_2 is considered to be precursors to form higher-order silanes. Main SiH_3 production processes in the SiH_4 plasmas are considered to be due to both the electron collisional dissociation of SiH_4 and hydrogen abstraction reaction. On the other hand, SiH_3 radicals that are not reactive are mostly lost by diffusion. Based on this fact, a triode SiH_4 plasma source with a multi-hollow geometry was proposed for fabrication of silicon films [29]. In fact, Hashimoto et al. [17] prepared amorphous silicon films at low pressure. To study the triode SiH_4 plasma source with a multi-hollow geometry, two-dimensional simulations of the multi-hollow SiH_4 plasma characteristics were carried out using the NIST-PML's rate

constant for removable of SiH_3. In this simulation, spatial profiles of various radicals as well as the plasma parameters were examined. To the best knowledge of the author, there is no report of the simulation of VHF SiH_4 plasmas using the rate constant of NIST-PML for the reaction (1.2). Comparison with the results for Perrin et al.'s rate constant was attempted.

3.1.2 Description of simulation model

To examine the VHF SiH_4/H_2 plasma in the multi-hollow geometry, the plasma hybrid module (PHM) of the PEGASUS Software [56] was used for the simulation. The detailed description of the PHM has been described in Chapter 2. A steady state of gas flow is calculated as the initial condition before the simulation of plasma. In the current model, the temperatures of ions and neutrals are fixed to a room temperature. For saving computation time, it is assumed that electrons have a Maxwellian velocity distribution, so the PHM is equivalent to a two-dimensional fluid model. Chemical reactions and their rate constants in the SiH_4/H_2 plasma are listed by Kushner [31]. The plasma chemistries are based on Kushner's article except for the following reaction (1.2).

Fig. (3.1) shows an illustration of the triode multi-hollow plasma source used in the simulation. Fig. (3.2) is then a schematic of used triode VHF plasma source with multi-hollow electrodes, where a substrate is positioned at a distance of 41 mm apart from the anode electrode. As shown in Fig. (3.2)(a), the periodic boundary for adjoining hollow electrodes is assumed. Simulation region is illustrated by two-dot chain lines.

As is well known, additional discharges can occur in the case of VHF discharges. To avoid such additional discharges, the balanced power feeding (BPF) method has been adapted to apply VHF powers to the discharge electrodes, anode and rod electrodes. The BPF was modeled according to [52]. Two VHF voltages, which have the same amplitude and the opposite phase ($\theta = 180°$) of each other, V_1 and V_2 are applied to the rod electrodes and anode electrodes, respectively:

$$\begin{aligned} V_1 &= V_{rf} cos(2\omega t) + V_{1dc} \\ V_2 &= V_{rf} cos(2\omega t + \theta) + V_{2dc} \end{aligned} \tag{3.1}$$

where V_{rf} is the amplitude of RF component of the applied voltages. Each voltage signal includes unfixed DC component V_{1dc} and V_{2dc}. When the BPF is used, the self-bias voltage is 0 V, which has been confirmed by measuring by an oscilloscope elsewhere [35]. Experimentally, to discharge electrodes power is applied using a power generator. Here, the power of 400 W is fed to the electrodes. As shown in Fig. (3.2), SiH_4/H_2 gas is introduced from a gas feeding tube behind the anode electrode with the flow rates of 200/200 sccm, respectively with the resulting pressure of 20 Pa. Sticking coefficients of SiH_3, SiH_2, and SiH radicals on the substrate and electrodes are important in silicon films growth. In the simulation, the sticking coefficients are assumed to be 0.1 for SiH_3, 0.8 for SiH_2, 0.8 for SiH, and 0.9 for Si [31]. In addition, those of higher-order silanes were assumed to be 1.0.

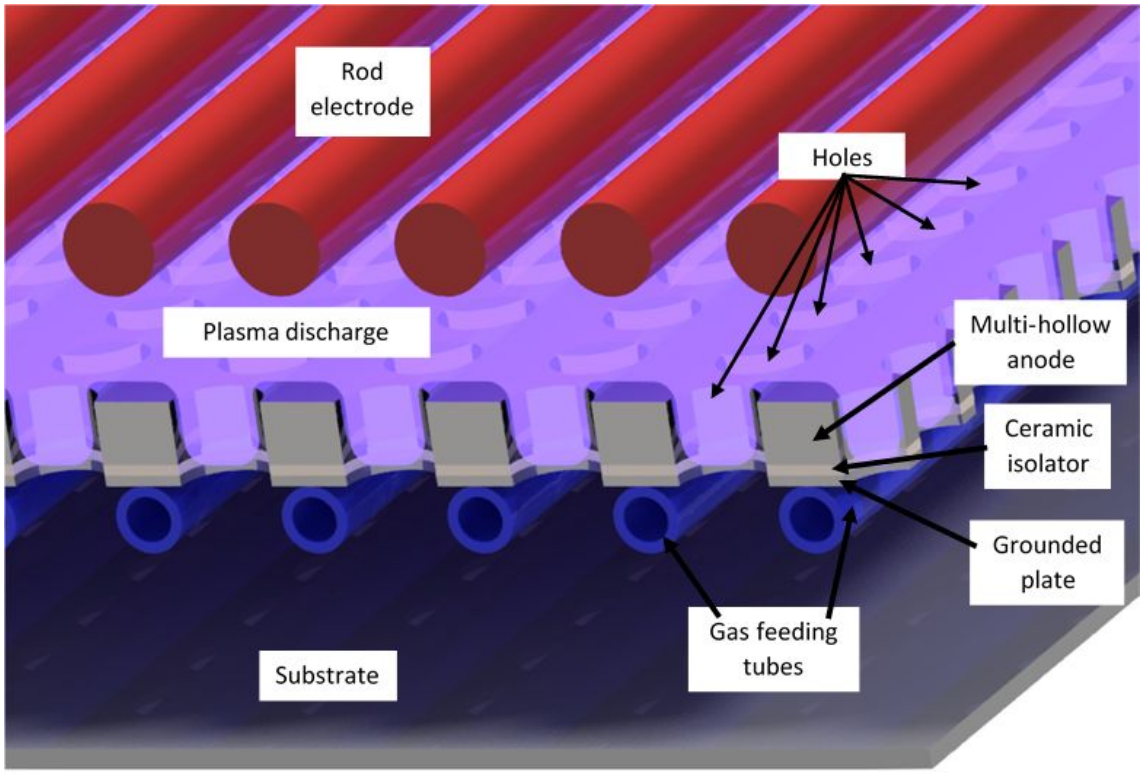

Figure 3.1: Illustration of triode multi-hollow plasma source.

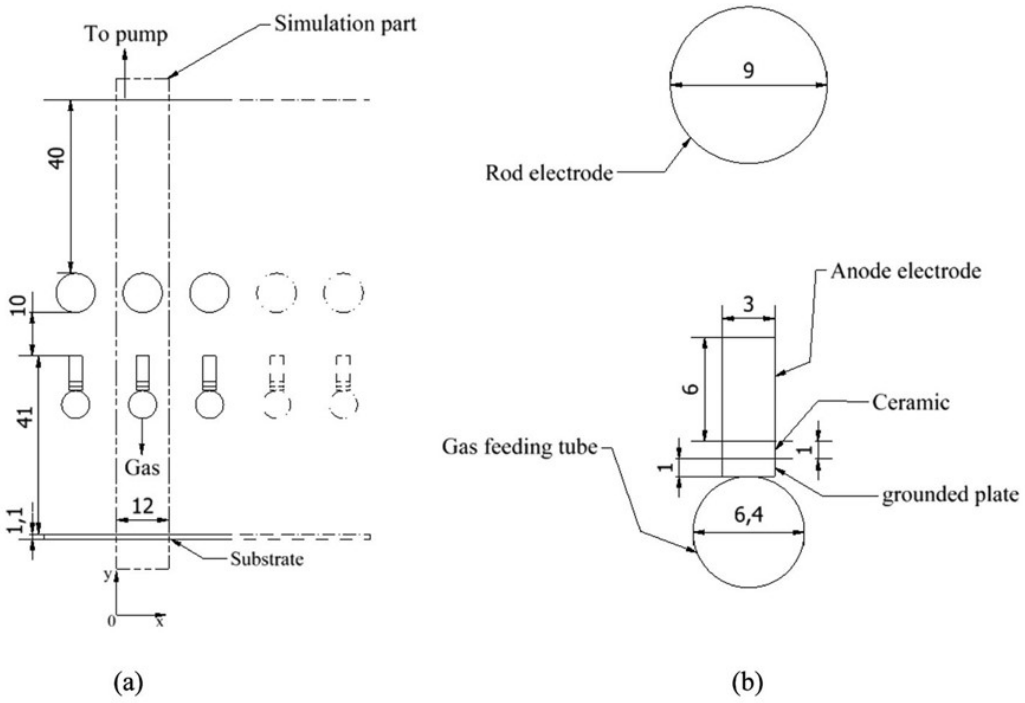

Figure 3.2: Schematic of (a) the triode multi-hollow plasma source and (b) detailed discharge electrodes, where the simulation domain is indicated by two-dot chain lines and the unit of the length is mm.

3.1.3 Results and discussion

At first, two-dimensional profiles of the plasma parameters such as the electron density n_e, SiH_3^+ and SiH_2^+ densities and electron temperature T_e were calculated. The simulation results are shown in figures (3.3-3.6). Fig. (3.3) shows that the maximum electron density is around $8.9 \times 10^{15}\,\mathrm{m}^{-3}$, while n_e near the substrate is approximately $9 \times 10^{13}\,\mathrm{m}^{-3}$. That is, n_e is very low near the substrate. As is well known, a CCP has a peak profile in electron density between two discharge electrodes. Fig. (3.3) also shows

that a spatial profile of n_e is different from that of a capacitively coupled plasma (CCP), which is considered owing to the configuration. As seen in Fig. (3.3)(b), the plasma of the electron density of 2×10^{15} m^{-3} is produced outside the rod electrodes, which is caused by the BPF method because the discharge electrodes have half a VHF voltage with the BPF method.

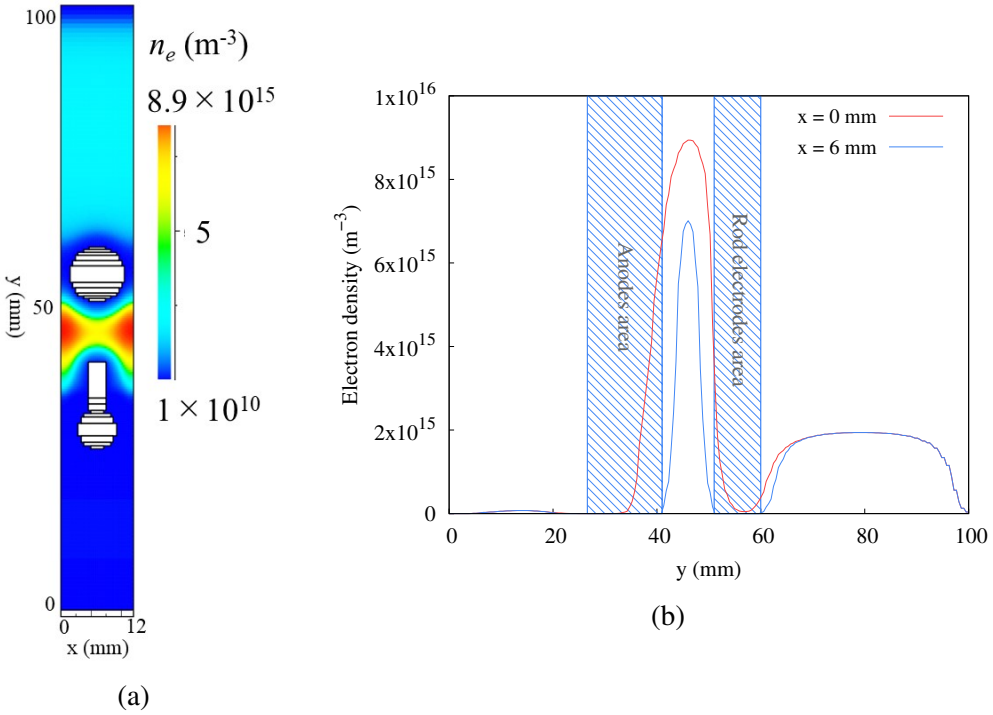

Figure 3.3: Electron density profile: (a) 2D map and (b) the density distribution at x = 0 and x = 6 mm, where the flow rate of SiH_4/H_2 gas and pressure are 200/200 sccm and 20 Pa, respectively. Blue area in (b) denotes the electrode positions at x = 6 mm.

Dominant ions in SiH_4 plasmas have been considered to be SiH_3^+. On the other hand, the rate constant of electron impact ionization of SiH_2^+ is comparable to that of SiH_3^+ [31]. The dominant ions were confirmed to be SiH_3^+. Fig. (3.4) shows that the maximum SiH_3^+ density 1.2×10^{16} m^{-3} and the spatial profile of the SiH_3^+ density is similar to that

of n_e, while the maximum SiH_2^+ density $\sim 1.6 \times 10^{15}$ m^{-3} that is one order of magnitude lower than the SiH_3^+ density.

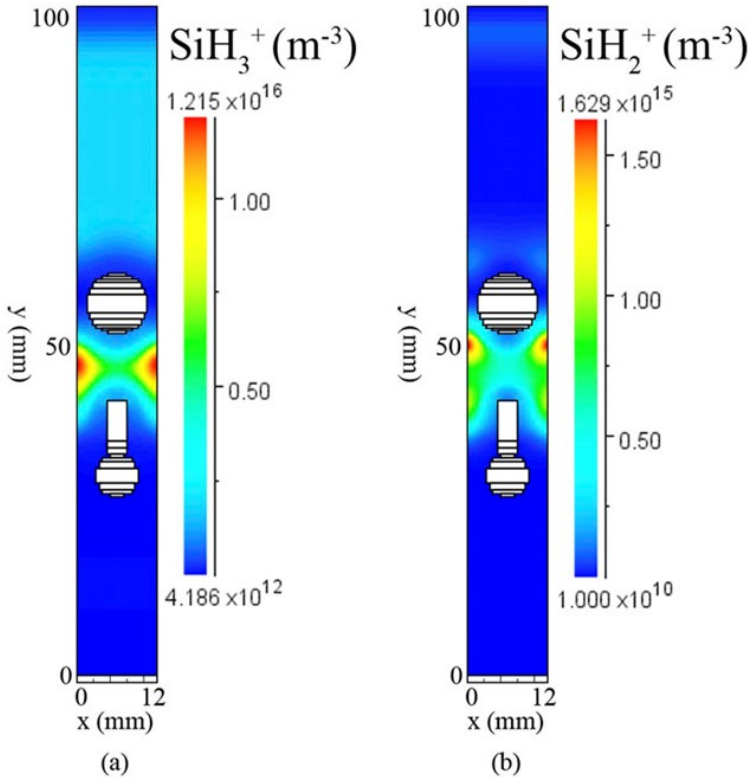

Figure 3.4: 2D maps of positive ion densities: (a) SiH_3^+ and (b) SiH_2^+ densities, where the flow rate of SiH_4/H_2 gas and pressure are 200/200 sccm and 20 Pa, respectively.

The electron temperature T_e is one of important parameters in the fabrication of amorphous silicon because T_e is proportional to the ion bombardment energy. Takai et al. [66] experimentally studied the effect of T_e on higher order silane formation in a VHF SiH_4/H_2 plasma (80 MHz) and found that H_2 gas dilution reduced T_e. Fig. (3.5) shows that T_e ~9 eV near the discharge electrodes and T_e ~2.5 eV near the center between the rod and

anode electrodes. The spatial profile of T_e is similar to the characteristic of the CCP H_2 plasma [7] where T_e is high near the discharge electrodes. Note that T_e is approximately 0.1 eV near the substrate. As already described in Chapter 1.1, the triode-PECVD provides high quality films, which is due to low T_e near the substrate.

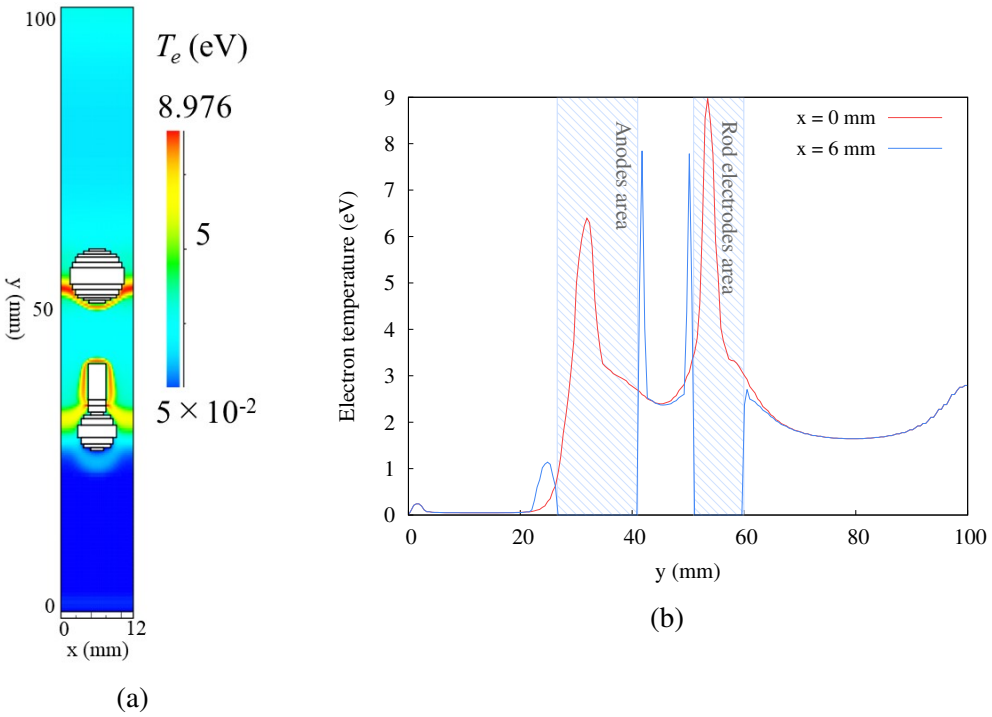

Figure 3.5: Electron temperature profile: (a) 2D map and (b) the electron temperature distribution at x = 0 and x = 6 mm, where the flow rate of SiH_4/H_2 gas and pressure are 200/200 sccm and 20 Pa, respectively. Blue area in (b) denotes the electrode positions at x = 6 mm.

As seen from Fig. (3.3) and (3.4), the SiH_3^+ density is a little higher than n_e, suggesting existence of negative ions. In fact, as shown in Fig. (3.6), the SiH_3^- density is comparable to n_e. The cross section of negative ion generation is not high compared with that of electron impact ionization, but negative ions are confined by the potential between two discharge electrodes, leading to an increase in the negative ion density. Note that

the spatial profile of the SiH_3^- density is similar to that of n_e, which is not understood physically. Looking at Fig. (3.3) to (3.6) carefully, it turns out that other positive and negative ions should exist to keep the charge neutrality.

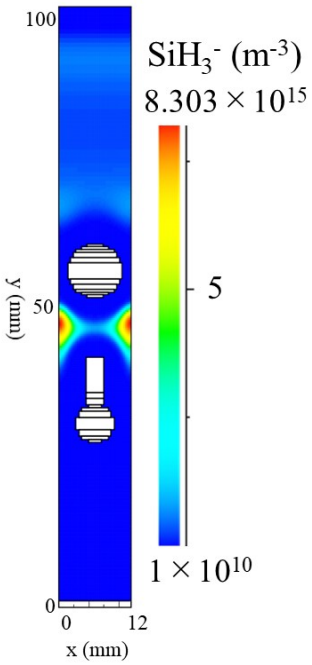

Figure 3.6: 2D map of the SiH_3^- density, where the flow rate of SiH_4/H_2 gas and pressure are 200/200 sccm and 20 Pa, respectively.

SiH_3 radicals in SiH_4 or SiH_4/H_2 plasmas are main contribution to amorphous silicon film. The simulation results for SiH_3, SiH_2 and SiH radical densities are shown in Fig. (3.7)(a), demonstrating that the maximum density of SiH_3 is around $1.5 \times 10^{19}\,m^{-3}$.The Fig. (3.8) shows the densities distributions of radicals SiH_3, SiH_2 and H. Note that the SiH_3 density near the substrate is $3 \times 10^{18}\,m^{-3}$, that is, the SiH_3 density near the substrate does not decrease rapidly, as shown later. This fact suggests that a high deposition rate can be expected. It was reported [31, 39] that when high quality amorphous silicon that pro-

vides a high conversion efficiency is fabricated, the density ratios SiH_3/SiH_2 and SiH_3/SiH are very high. Fig. (3.8) indicates that although the density ratio SiH_3/SiH_2 near the center is around 10, this ratio near the substrate is ~ 100. Kushner [31] reported the density ratio $SiH_3/SiH_2 \sim 100$ at the center of CCP. This difference near the center is attributed to the use of the different rate constant for Eq. (1.2) [31]. Thus, it can be concluded from the results of this simulation that the triode-PECVD using the VHF multi-hollow geometry will be suitable for the fabrication of high quality amorphous silicon with a fast deposition. Fig. (3.8) also shows that the spatial profile of the SiH, SiH_3 and SiH_2 densities between the anode and rod electrodes is similar to that of n_e . To explain this result, more detail simulations are necessary.

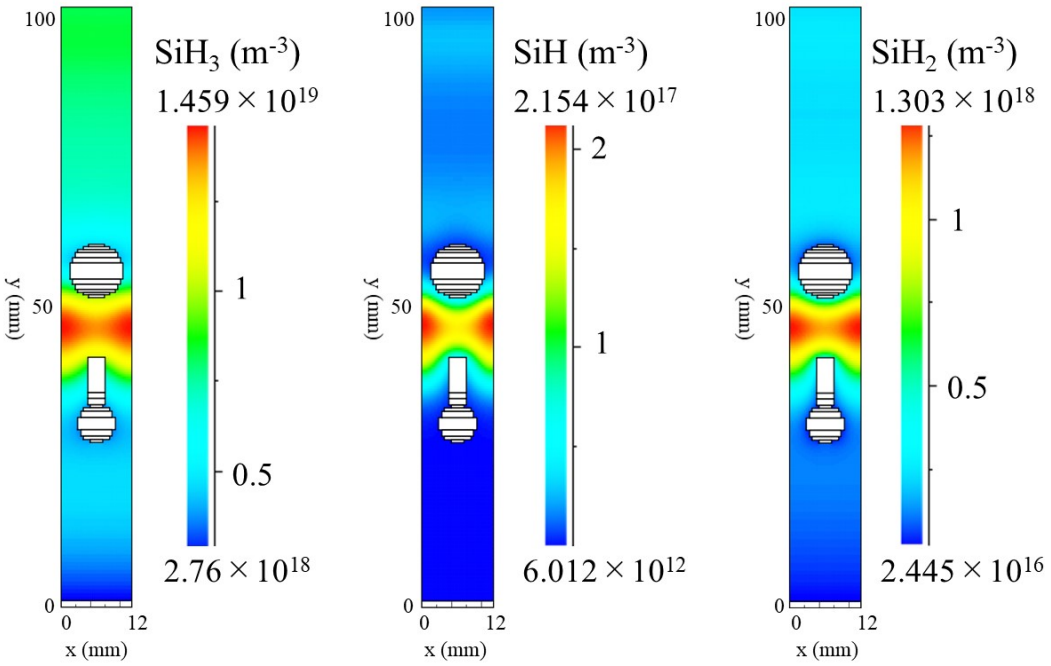

(a) 2D maps of SiH_3 (b) 2D maps of SiH (c) 2D maps of SiH_2

Figure 3.7: 2D maps of radical densities of (a) SiH_3, (b) SiH and (c) SiH_2, where the flow rate of SiH_4/H_2 gas and pressure are 200/200 sccm and 20 Pa, respectively.

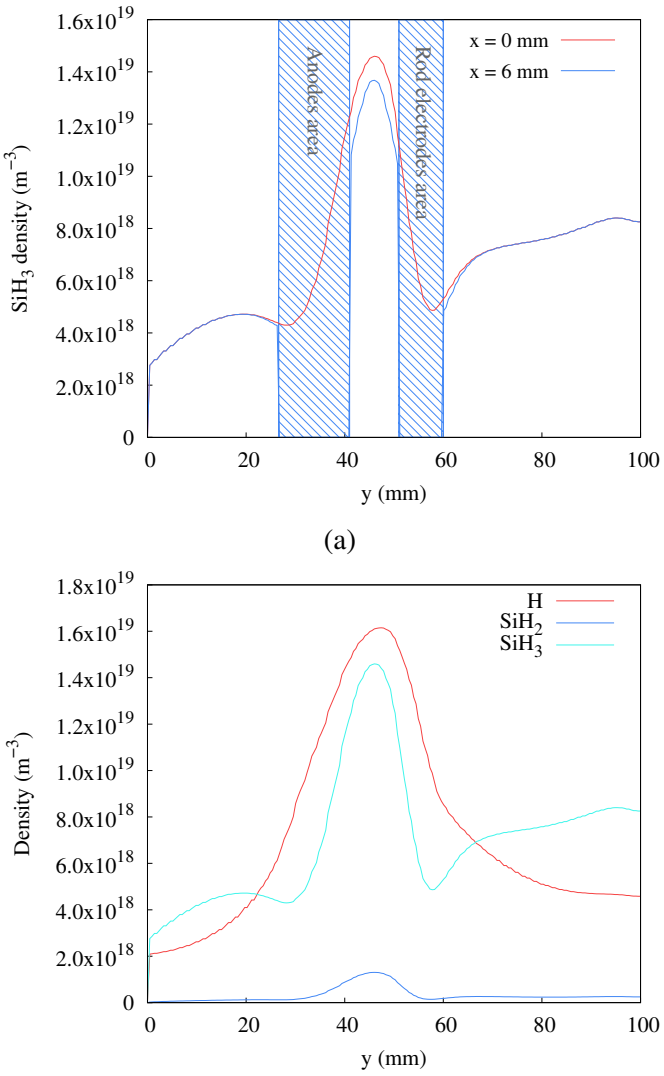

Figure 3.8: Radical densities distribution: (a) SiH_3 density distribution at x = 0 and 6 mm and (b) SiH_3, SiH_2, and H density distributions at x = 0 mm. Here, the flow rate of SiH_4/H_2 gas and pressure are 200/200 sccm and 20 Pa, respectively. Blue area in (a) denotes the electrode positions at x = 6 mm.

As is well known, the multi-hollow discharge can realize a high-electron density plasma by hollow effect [24, 54]. However, as shown in Fig. (3.3), $n_e \sim 10^{16}\,\mathrm{m}^{-3}$ that is a typical density of CCP. To confirm the hollow effect the anode size was changed

from 3 mm to 9 mm in diameter, but the plasma characteristics were almost the same. To get a higher-electron density plasma, it is necessary to examine the detailed pressure dependence of the plasma parameters [24, 54]. In fact, the hollow effect was observed at relatively high pressures above 266 Pa [24].

Higher order silanes are generated by successive insertion reactions [39, 41, 66] of SiH_2 starting from $SiH_2 + SiH_4 \longrightarrow Si_2H_6$, $SiH_2 + Si_2H_6 \longrightarrow Si_3H_8$,..... to $SiH_2 + Si_{n-1}H_{2n} \longrightarrow Si_nH_{2n+2}$. In the simulation the two-dimensional spatial profiles of Si_2H_6 and Si_3H_8 radicals were calculated. Fig. (3.9) shows that the densities of Si_2H_6 and Si_3H_8 are uniform between two electrodes and are of order of $10^{20}\,m^{-3}$. As seen from Fig. (3.9), both radicals do not decrease rapidly like SiH_3. It is reported that Si_2H_6 and Si_3H_8 radicals do not contribute to the film quality [39, 41]. However, as seen in Fig. (3.11), the Si_5H_{12} and Si_4H_{10} densities near the substrate is comparable to the SiH_3 density. Fig. (3.12) shows spatial profiles of Si_4H_{10} and Si_5H_{12} densities at x = 0 and 6 mm, where the flow rate of SiH_4 / H_2 gas and pressure are 200/200 sccm and 20 Pa, respectively. Figures (3.11) and (3.12) strongly suggest dust formation [11, 12].

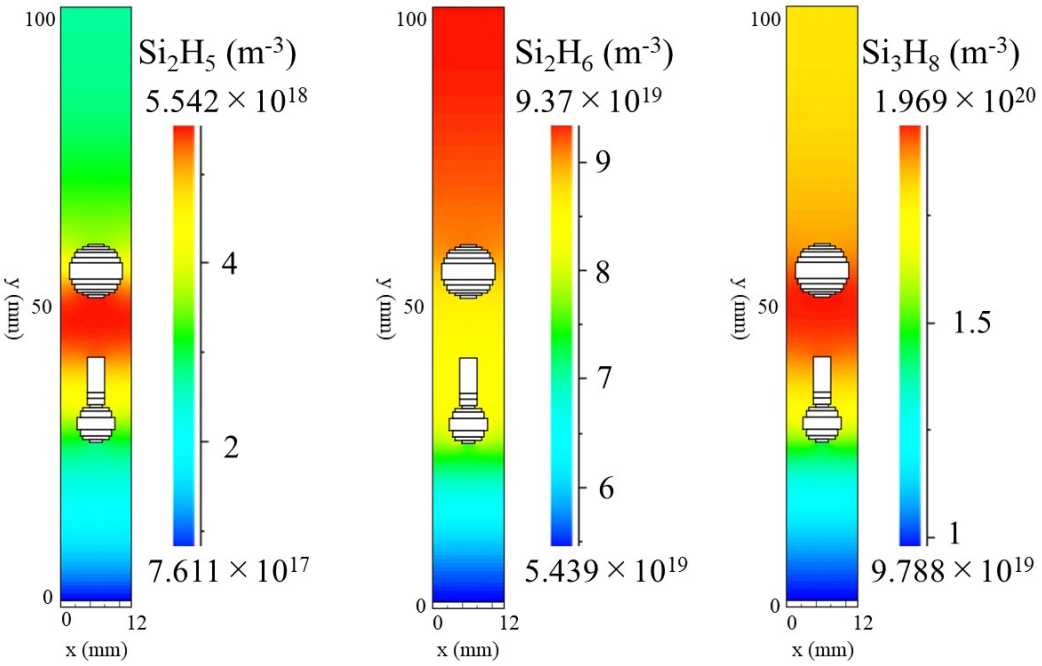

(a) 2D map of Si_2H_5 (b) 2D map of Si_2H_6 (c) 2D map of Si_3H_8

Figure 3.9: Higher order silane densities: 2D map of (a) Si_2H_6, (b) Si_2H_5 and (c) Si_3H_8 densities, where the flow rate of SiH_4/H_2 gas and pressure are 200/200 sccm and 20 Pa, respectively.

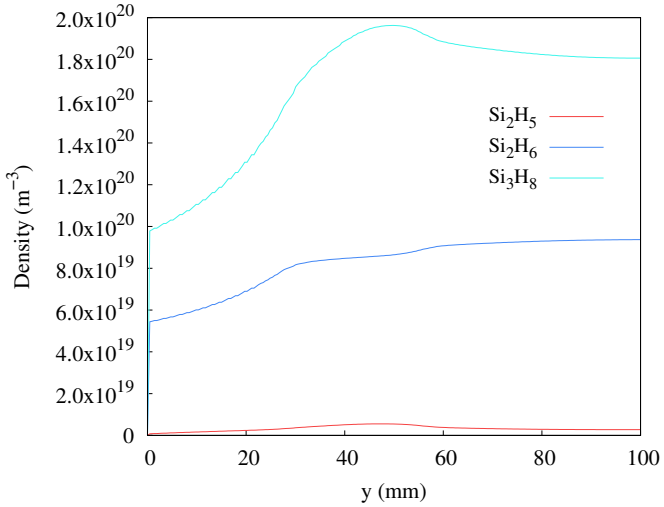

(a)

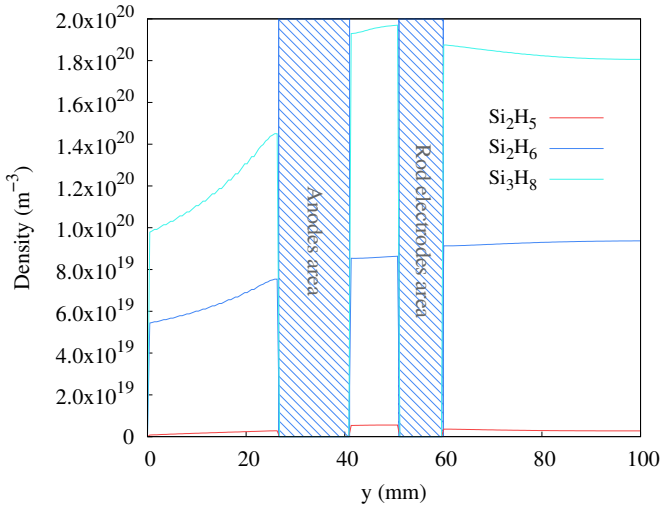

(b)

Figure 3.10: Higher order silane densities: spatial profiles of Si_2H_6, Si_2H_5 and Si_3H_8 densities at(a) x = 0 and (b) 6 mm, where the flow rate of SiH_4/H_2 gas and pressure are 200/200 sccm and 20 Pa, respectively. Blue area in (b) denotes the electrode positions at x = 6 mm.

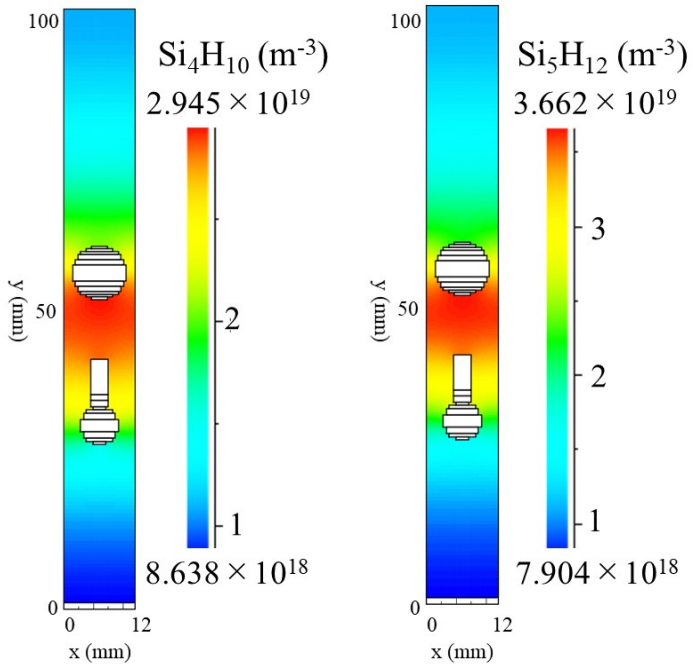

(a) (b)

Figure 3.11: Higher order silane densities: (a) spatial profiles of Si_4H_{10} and Si_5H_{12} densities at x = 0. (b) spatial profiles of Si_4H_{10} and Si_5H_{12} densities at x = 6 mm, where the flow rate of SiH_4/H_2 gas and pressure are 200/200 sccm and 20 Pa, respectively.

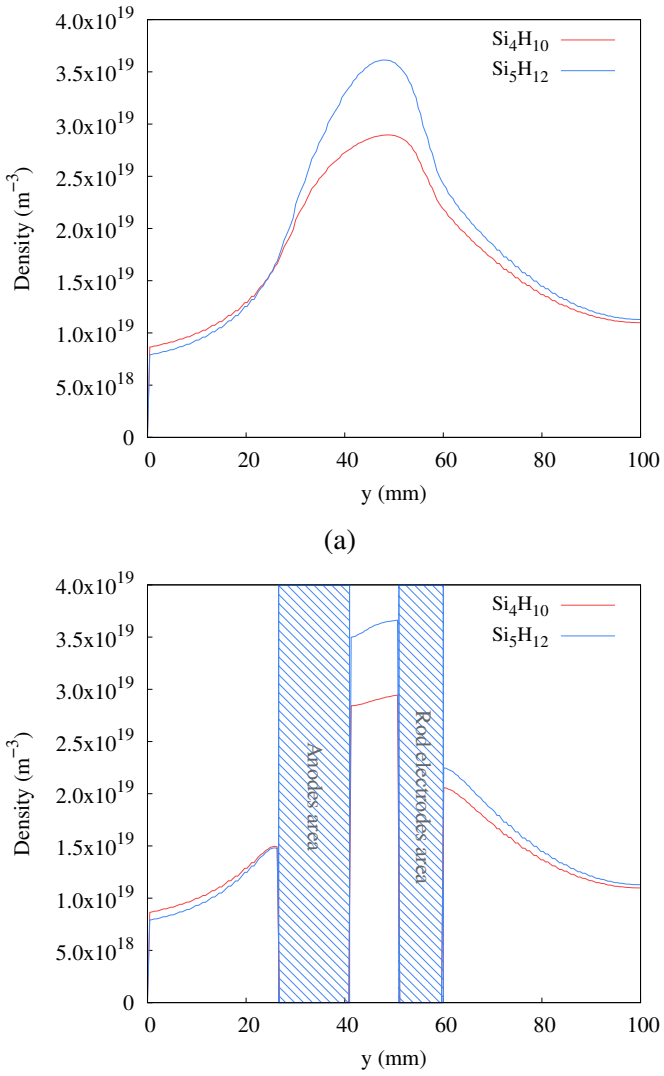

Figure 3.12: Higher order silane densities: (a) spatial profiles of Si_4H_{10} and Si_5H_{12} densities at x = 0. (b) spatial profiles of Si_4H_{10} and Si_5H_{12} densities at x = 6 mm, where the flow rate of SiH_4/H_2 gas and pressure are 200/200 sccm and 20 Pa, respectively. Blue area in (b) denotes the electrode positions at x = 6 mm.

Hydrogen atoms also play an important role in amorphous silicon film growth because SiH_3 radicals are produced by the hydrogen abstraction as well as the electron impact dissociation. The simulated results of the hydrogen atom density (H density) are shown

in Fig. (3.13). As seen in Fig. (3.13)(a), the H density is uniform between two discharge electrodes, amounting to $\sim 1.6 \times 10^{19}\,\mathrm{m}^{-3}$ that is comparable to the SiH_3 density. Note that the H density $\sim 2.2 \times 10^{18}\,\mathrm{m}^{-3}$ at the substrate. To look at a detailed spatial profile of the H density near the electrodes, the profile is plotted at x = 6 mm in Fig. (3.13)(b), representing that the H density decreases near the discharge electrodes and 0 at the surface of the electrodes. This is due to the sticking coefficient of 1.0 for H atoms on the electrodes.

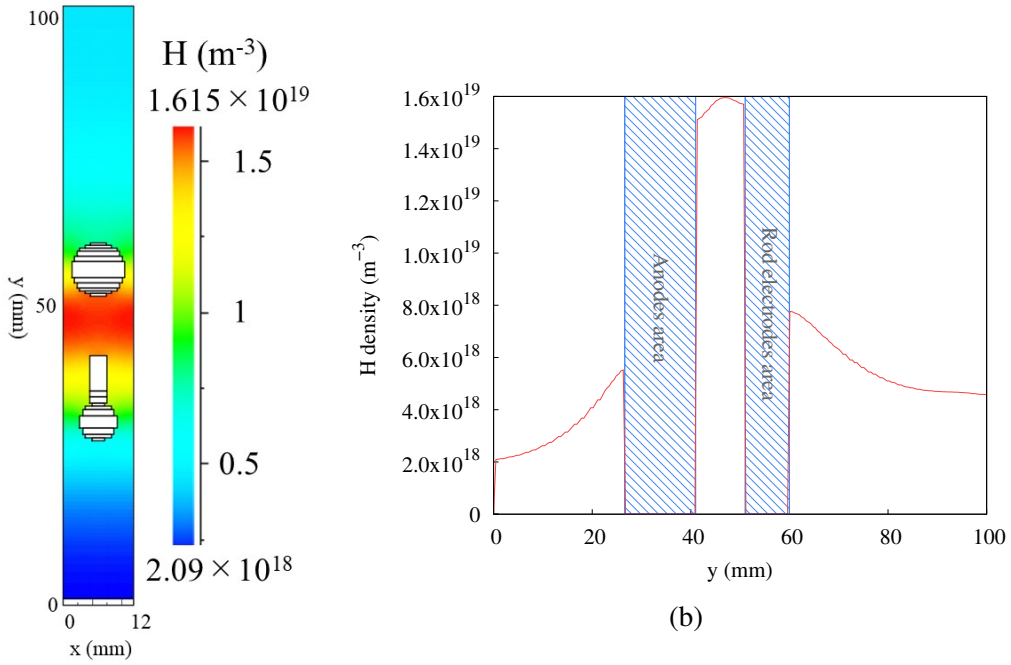

Figure 3.13: The H atom density: (a) 2D map and (b) spatial profile at x = 6 mm, where the flow rate of SiH_4/H_2 gas and pressure are 200/200 sccm and 20 Pa, respectively. Blue area in (b) denotes the electrode positions at x = 6 mm.

Kushner [31] explains that the electron impact dissociation dominates SiH_3 radical production near the discharge electrode and the hydrogen abstraction is more dominant near the center of the reactor. Rehman et al. [3] reported that the hydrogen abstraction

is dominant in SiH_3 radical generation at torr-region pressures. From the simulation it is difficult to judge which effect is dominant in SiH_3 radical generation between two discharge electrodes. In addition, T_e near the substrate is too low to generate SiH_3 radicals by the electron impact dissociation. It is concluded from above discussions that radicals such as SiH_3, SiH_2 and SiH are produced between the discharge electrodes and diffuse to the substrate.

The plasma characteristics was also simulated using the Perrin et al.'s rate constant. The results near the center and substrate are shown in Table (3.1). The densities of various species are mostly same, while the SiH_3 density is low compared with the NIST-PLM's case. That is, the rate constant of the reaction (1.2) affects the SiH_3 radical generation. Note that the electron density is nearly equal to the $SiH_3{}^+$ density, meaning that negative ions are negligible small. In fact, the $SiH_3{}^-$ density was lower than 1×10^{15} m^{-3} between two discharge electrodes. When many negative ions exist, T_e tends to increase. Simulation results indicate that T_e was as low as 1 eV. In addition, as seen from Table (3.1), the density ratio SiH_3/SiH_2 ~50 while it is around 10 for NIST's rate constant. Bleecker et al. [12] reported the one-dimensional simulation of a SiH_4 CPP and found that many dusts were generated, where the density ratio SiH_3/SiH_2 ~100. These results suggest that the density ratio SiH_3/SiH_2 is one of measures to describe film quality, but it is not sufficient.

To validate the simulation results, the comparison with the experiments is important.

A measurement of the parameters of a VHF SiH_4/H_2 plasma produced with the multi-rods electrode was conducted [68, 73], where a heated Langmuir probe was used to prevent contaminations. It was found that the plasma parameters depended on the dilution rate of H_2, pressure and power, where the SiH_3^+ ion density was estimated from the ion saturation current of the Langmuir I-V curves. Typically, the SiH_3^+ density $\sim 10^{15}\,\mathrm{m}^{-3}$ and T_e ~2.5 eV [28], which are qualitatively in agreement with the simulation results. In the simulation many negative ions in the plasma were also observed [73]. SiH_4-CCP based depositions are also important for semiconductor fabrication (e.g., SiO_2, Si_3N_4) [28, 32]. In this Chapter an electron velocity distribution function was not calculated, and for the simplicity it was assumed that electrons have a Maxwellian velocity distribution function. As is well known, stochastic heating [34] occurs in CCP at low pressures and, as a result, electrons have a bi-Maxwellian velocity distribution function, which might change plasma processing. Simulations considering the electron velocity distribution function is a future study.

To simulate the characteristics of a triode SiH_4/H_2 plasma using a multi-hollow type source the two-dimensional PHM of PEGASUS was used. Here, it is assumed that the spatial distribution of radicals is completely uniform in the direction (z-axis) perpendicular to the page. In an actual system, the plasma is not uniform along the z-axis. Three-dimensional simulations [10, 24] are necessary for designing the multi-hollow plasma source. On the other hand, as is well known, there are many chemical reactions

Table 3.1: Densities of various species for different positions: (a) maximum densities near the center and (b) densities near the substrate, at x = 0 mm and y = 3 mm, where the unit of densities is m^3, and k_p and k_n are the rate constants derived by Perrin et al. and NIST-PML.

(a)									
(m^{-3})	*ne*	SiH_3^+	SiH_2^+	SiH_3	SiH_2	SiH	H	Si_2H_6	Si_3H_8
k_p	4.6×10^{16}	3.7×10^{16}	2.3×10^{15}	6.0×10^{18}	1.2×10^{17}	2.9×10^{16}	5.4×10^{18}	6.6×10^{19}	3.6×10^{19}
k_n	8.9×10^{15}	1.2×10^{16}	1.6×10^{15}	1.5×10^{19}	1.3×10^{18}	2.2×10^{17}	1.6×10^{19}	9.4×10^{19}	2.0×10^{20}
(b)									
(m^{-3})	*ne*	SiH_3^+	SiH_2^+	SiH_3	SiH_2	SiH	H	Si_2H_6	Si_3H_8
k_p	2.6×10^{13}	2.7×10^{13}	1.0×10^{10}	2.2×10^{18}	8.1×10^{15}	5.9×10^{12}	8.2×10^{17}	4.2×10^{19}	2.1×10^{19}
k_n	9.7×10^{10}	5.7×10^{12}	1.0×10^{10}	3.2×10^{18}	4.6×10^{16}	1.2×10^{13}	2.1×10^{18}	5.6×10^{19}	1.0×10^{20}

in SiH_4/H_2 plasmas. So, it is necessary to include many reactions into the simulation. The purpose is to design a VHF plasma source that can provide high quality amorphous silicon with a high speed deposition. This will be realized by a triode plasma produced with the multi-hollow plasma source that is essentially necessary. Actual 3D simulation was not possible with the present PEGASUS software. Nonetheless, the two-dimensional simulations still help for the understanding of the characteristics of VHF SiH_4/H_2 plasmas because there is less information about the spatial distributions of Si related radicals. Here, the focus was on the characteristics of the triode SiH_4/H_2 plasma. In fact, the solar cell industries [26] have divided the discharge electrodes to avoid the two-dimensional standing wave and other electromagnetic effects.

As already mentioned, a typical VHF plasma of a high electron density with a low electron temperature between two discharge electrodes was obtained. However, the multi-hollow effect [31] was not found, so the pressure was increased. The density ratio SiH_3/SiH_2 that was commonly used as a judgement of film quality was around 10 at the center, while it was 70 near the substrate. Here, the SiH_3 density was $1.5 \times 10^{19}\ m^{-3}$ at the center and $3.2 \times 10^{18}\ m^{-3}$ near the substrate. These results may indicate the fabrication of high quality amorphous silicon. However, as seen in Fig. (3.11a) and (3.12), the Si_5H_{12} density near the substrate is comparable to the SiH_3 density, suggesting dust formation.

3.1.4 Conclusions

A triode VHF SiH_4/H_2 plasma with the multi-hollow geometry was simulated using PEGASUS PHM. The following results were found:

(1) A typical VHF plasma of high n_e and low T_e is produced between two discharge electrodes, anode and rods electrodes, while n_e near the substrate is much lower than that between the discharge electrodes.

(2) The rate constant of $SiH_3 + SiH_3 \longrightarrow SiH_2 + SiH_4$ affects generation of SiH_3 radicals.

(3) Preferable characteristics of a high SiH_3 density and a low electron temperature near the substrate are found. Many negative ions exist.

(4) The ratio of SiH_3/SiH_2 and SiH_3/SiH near the substrate is very high.

(5) The Si_5H_{12} density near the substrate is comparable to the SiH_3 density.

In summary, even though the found characteristics math a typical VHF plasma, the multi-hollow effect [54] was not detected. It might appear at higher pressures. Furthermore, the SiH_3 density is comparable to the Si_5H_{12} density near the substrate, which means that dust particles are formed, suggesting lower quality film at selected pressure. It is concluded that the multi-hollow plasma source is not suitable for fabrication of amorphous silicon. In fact, Hashimoto et al. [17] introduced a dust filter to prepare high-quality amorphous silicon films although the dust filter made the deposition rate lower.

3.2 Multi-Rod electrodes plasma

3.2.1 Introduction

The development of a new triode plasma source that enables a high-speed deposition is required by solar cell industries. To contribute to the development of the triode plasma source, two-dimensional simulations of a triode VHF SiH_4 plasma using multi-rod electrodes [25] with the plasma hybrid code of the PEGASUS software [7, 8, 52, 53, 56] was performed.

Kawai et al. [25] investigated ladder shaped electrode (multi-rod) for silicon films by VHF-PECVD. They found out that the VHF discharge frequency of 60 MHz was relatively uniform compared to those with 80 MHz and 100 MHz also investigated in their work. In this simulation the frequency was selected at 60 MHz as well to follow the relatively high stability of the plasma discharge. In fact, Takatsuka et al. [67] succeeded in the fabrication of amorphous silicon films with an area of 1 m^2 using the multi-rod electrodes. In this chapter, plasma production with the pressure of 6.7, 13.3, 26.6, and 66.7 Pa were simulated to study the pressure dependence of n_e, T_e and higher-order silane densities.

3.2.2 Description of simulation model

As described in Chapter 2, the current simulation has introduced the balanced power feeding (BPF) method [9, 47] to produce a VHF plasma. A 3D projection of the triode

system is depicted in Fig. (3.14).Fig. (3.15) then shows a schematic of triode VHF plasma source used in this 2D simulation with multi-rod electrodes (staggered electrodes), where a substrate (dielectric constant, 3.8; thickness, 2 mm) is positioned 25 mm away from the lower rod electrodes to realize triode PECVD. The discharge gap distance d is 10 mm. As shown in Fig. (3.15), the periodic boundary for adjoining rod electrodes using Cartesian coordinates was assumed, (x-y). The simulation region is illustrated by two-dot chain lines. The BPF was modeled according to Ogiwara et al. [52]. Two VHF voltages with the same amplitude but opposite phases, , V_1 and V_2 are applied to the upper and lower rod electrodes of 10 mm diameter, respectively:

$$\begin{aligned} V_1 &= V_{rf} cos(2\omega t) + V_{1dc} \\ V_2 &= V_{rf} cos(2\omega t + \theta) + V_{2dc} \end{aligned} \tag{3.2}$$

where f and V_{rf} are the frequency and amplitude of the VHF voltages, respectively. When the voltages V_{1dc} and V_{2dc} are applied to the upper and lower rod electrodes, a SiH_4 plasma is produced by VHF discharge. Generally, DC biases of each electrode, V_{1dc} and V_{2dc}, vary self-consistently, with the assumption that blocking capacitors are connected to the discharge electrodes. When the BPF method is used, the self-bias voltage is 0 V, which has been confirmed using an oscilloscope [36]. The frequency is 60 MHz and the pressure is 13.3 Pa. The applied voltages are $V_1 = V_2 = 50$ V.

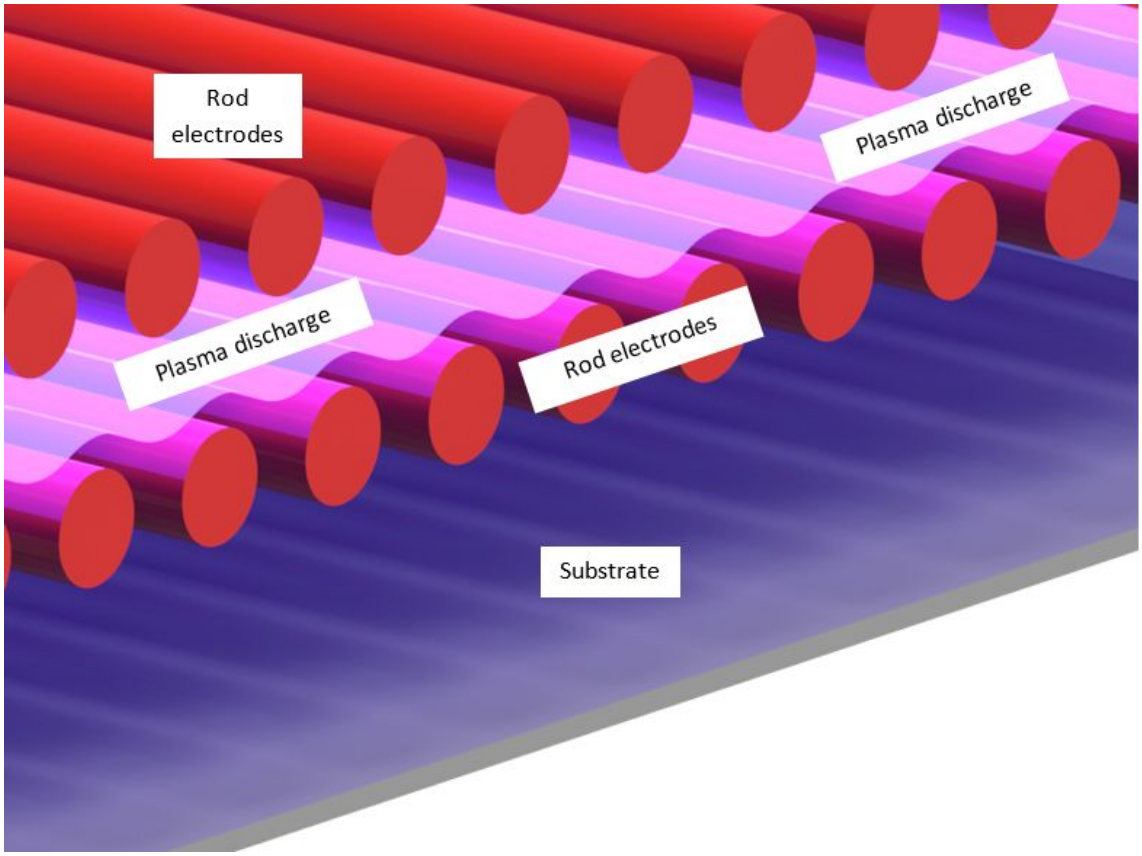

Figure 3.14: Illustration of the triode multi-rod plasma source.

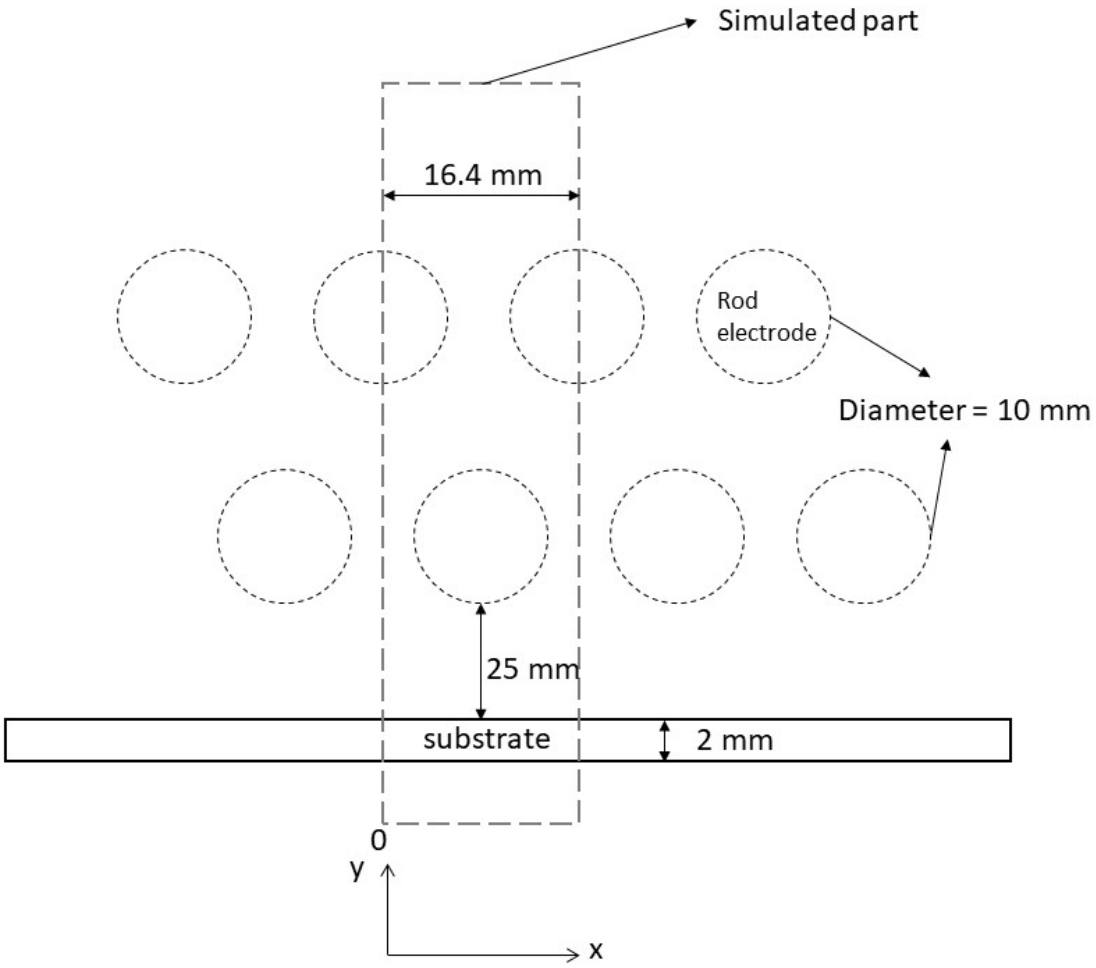

Figure 3.15: Schematic of a triode multi-rod plasma source. The two-dot chain lines indicate the boundaries of the simulation domain.

3.2.3 Results and discussion

Firstly, two-dimensional maps of the plasma parameters including negative and positive ions were examined. As can be seen in Fig. (3.16)(a), the electron density n_e is around $1 \times 10^{16}\,\mathrm{m}^{-3}$ at the center while n_e near the substrate is much lower than that inside the discharge electrodes; n_e is around $1 \times 10^{13}\,\mathrm{m}^{-3}$ at a location 3 mm away from

the substrate (y = 15 mm), as expected. As is well known, there are many negative ions in a SiH_4 plasma, which will serve as precursors of dust [12]. In the simulation the densities of SiH_3^- and H^- which are considered to be the main negative ions in SiH_4 plasmas were calculated. Fig. (3.16)(b) shows that the SiH_3^- density is $5.6 \times 10^{15}\,m^{-3}$, which is lower than n_e, but it is not negligibly small. On the other hand, the H^- density is $\sim 3.6 \times 10^{12}\,m^{-3}$, which is negligibly small in this plasma.

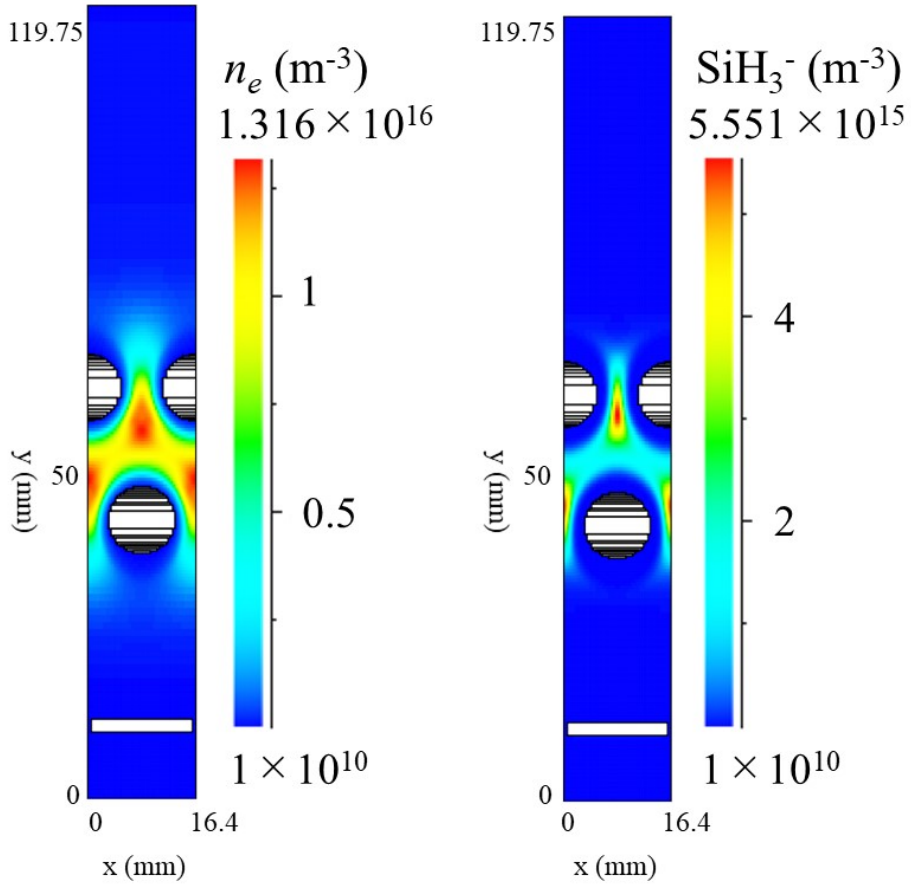

Figure 3.16: Density profiles of (a) electrons n_e and (b) SiH_3^- ions at a pressure of 13.3 Pa.

Dominant ions in a SiH_4 plasmas have been considered to be SiH_3^+. As Kushner

[31] reported, the electron impact ionization cross section of SiH_2^+ is comparable to that of SiH_3^+ and there are many positive ions in addition to both positive ions in a SiH_4 plasma. Fig. (3.17) shows that the SiH_3^+ density is higher than the SiH_2^+ density between the discharge electrodes. The densities of higher-order ions such as $Si_2H_5^+$ and $Si_3H_6^+$ were also calculated and found that they were comparable to the SiH_2^+ density. Thus, the dominant ions were confirmed to be SiH_3^+ in the SiH_4 plasma. Note that the spatial profiles of positive ions calculated here were similar.

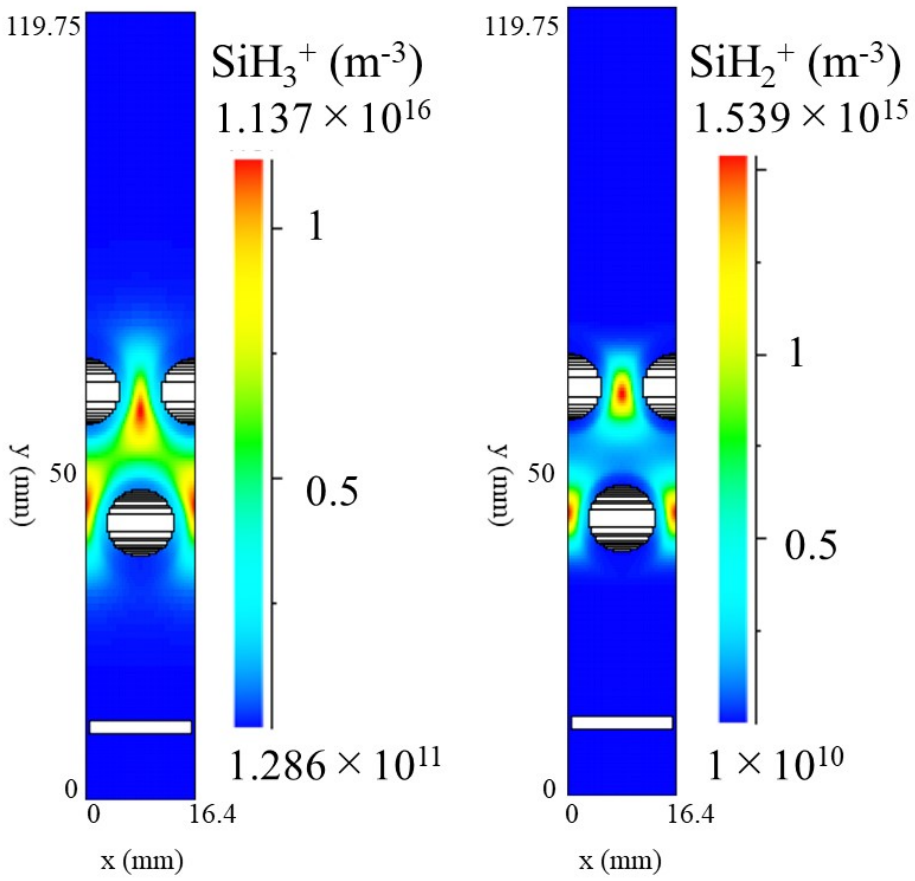

Figure 3.17: Density profiles of (a) electrons SiH_3^+ and (b) SiH_2^+ ions at a pressure of 13.3 Pa.

As described in Chapter 1.1, the electron temperature T_e is an important parameter in the fabrication of amorphous silicon. The spatial profiles of T_e and the plasma potential V_s is plotted in Fig. (3.18). As seen in Fig. (3.18)(a), T_e is uniform (~2 eV) except around the discharge electrodes (T_e= 5.5 eV), which is a typical characteristic of the CCP [7, 8, 52, 53]. Fig. (3.18)(b) exhibits that V_s is uniform between the discharge electrodes and an ambipolar field is formed outside them. Note that T_e =1.8 eV and V_s = 34.2 V at y = 15 mm (near the substrate).

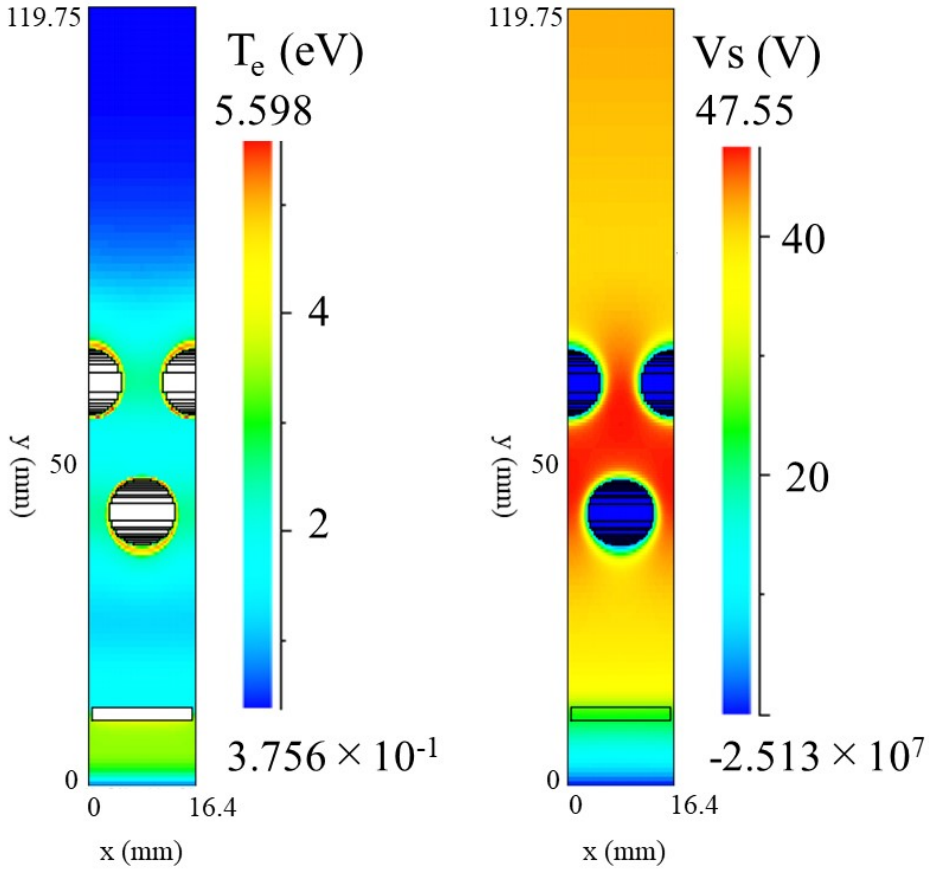

Figure 3.18: Spatial profiles of (a) the electron temperature T_e and plasma potential V_s at a pressure of 13.3 Pa.

As is well known, the deposition rate and quality of amorphous silicon are affected by SiH_3, SiH_2, SiH, and H radicals. The 2D maps of these radicals are plotted in Fig. (3.19), showing that the SiH_3 density is 2.5×10^{19} m^{-3} near the center, which is much higher than the SiH_2 and SiH densities. Note that, although n_e is very low near the substrate, the SiH_3 density near the substrate is relatively high, suggesting a high deposition rate. Matsuda et al. [41] described that, when high-quality amorphous silicon was prepared, the SiH_3 density was three orders of magnitude higher than the SiH_2 density, and Kushner

[31] also reported similar results in the simulation. In this case, the maximum density ratio SiH_3/SiH_2 is equal to 25, which is smaller than Kushner's result, as discussed later. Kushner [31] studied spatial density profiles of SiH_3, SiH_2, and SiH radicals in detail and found that the SiH_3 density is fairly uniform between two parallel discharge electrodes, while the SiH_2 and SiH densities have a peak close to the discharge electrodes because SiH_2 and SiH are mainly produced by electron impact dissociation.

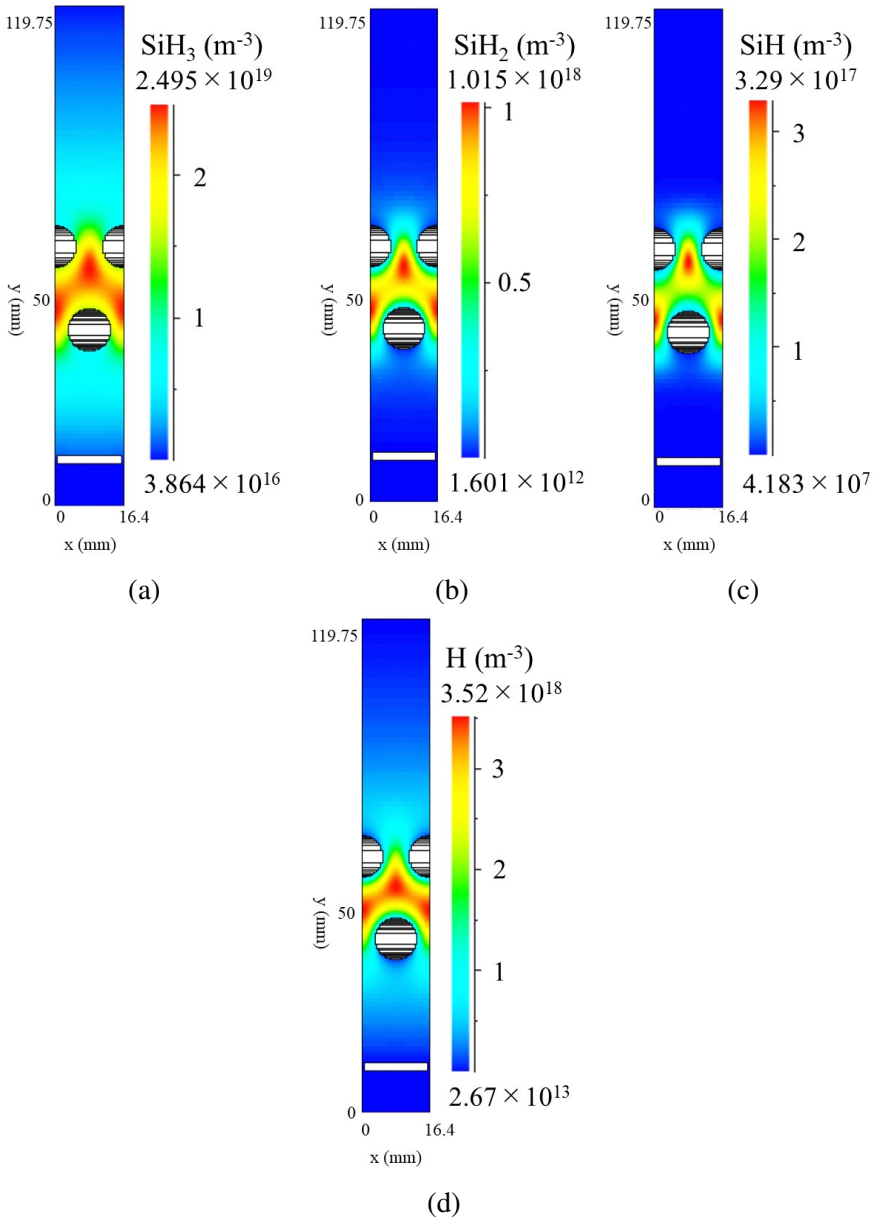

Figure 3.19: Spatial profiles of radical densities: (a) SiH_3, (b) SiH_2, (c) SiH, and (d) H densities, where the pressure is 13.3 Pa.

In Fig. (3.20), the axial profiles of the SiH_3, SiH_2, and SiH densities at x = 0 mm are plotted. These densities at y = 57-67 mm are 0. Fig. (3.20) shows that the SiH_3 density is uniform between the discharge electrodes, which is considered to be due to

the generation of SiH_3 by hydrogen abstraction as well as electron impact dissociation [31]. H radicals are also sensitive to the deposition rate [31]. Fig. (3.19)(d) shows that the H density has a spatial profile similar to the SiH_3 density, suggesting that hydrogen abstraction contributes to the the production of the plasma. The H density near the center is around $3.5 \times 10^{18}\,\mathrm{m}^{-3}$, which is one order of magnitude higher than that of a dust plasma [12]. Fig. (3.20) also shows that the density ratio SiH_3/SiH_2 is equal to 100 near the substrate. Note that the SiH_2 and SiH densities decrease faster than the SiH_3 density outside the discharge electrodes. Their diffusion coefficients are almost the same; thus, the difference is due to the sticking coefficients on the substrate, as Kushner pointed out in his article [31].

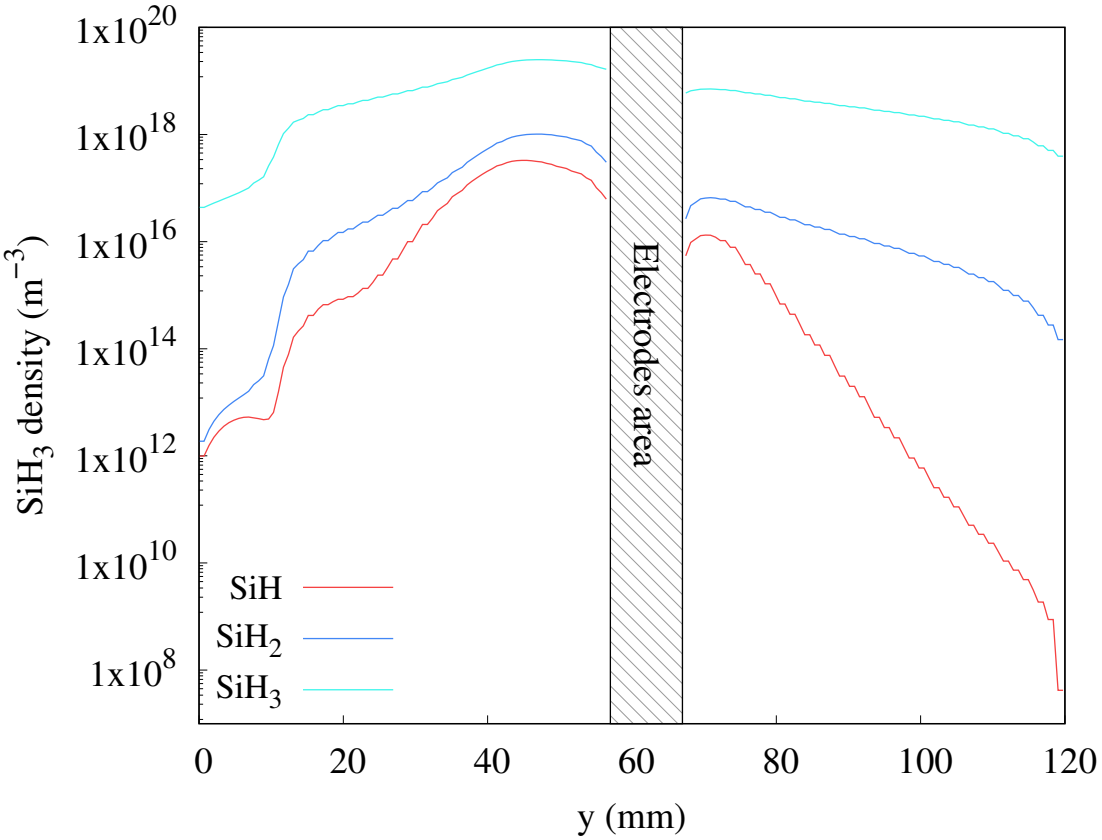

Figure 3.20: Spatial distributions of SiH, SiH_2, and SiH_3 densities at x = 0 at a pressure of 13.3 Pa. No plasma is produced at y = 57-67 mm corresponding to the discharge electrodes.

Higher-order silanes are produced by successive insertion reactions of SiH_2 starting from $SiH_2 + SiH_4 \longrightarrow Si_2H_6$, $SiH_2 + Si_2H_6 \longrightarrow Si_3H_8$,..... to $SiH_2 + Si_{n-1}H_{2n} \longrightarrow Si_nH_{2n+2}$. Density profiles were calculated for important higher-order silanes, Si_nH_{2n+2} molecules, and $Si_{n-1}H_{2n}$ radicals, where the integer n = 2-5. The results are shown in Fig. (3.21) and (3.22). As seen from Fig. (3.21) and (3.22), it seems that higher-order silanes have similar spatial profiles that are different from those of charged particles. The higher-order silanes are uniform compared with the SiH_2 density at the center of the discharge electrodes. The molecular densities at the center are $1.2 \times 10^{19}\,m^{-3}$ for

Si_2H_6, $6 \times 10^{17}\,m^{-3}$ for Si_3H_8, $5 \times 10^{15}\,m^{-3}$ for Si_4H_{10}, and $3.6 \times 10^{13}\,m^{-3}$ for Si_5H_{12}. As seen from Fig. (3.21) and (3.22), the molecular densities near the substrate are two orders of magnitude lower than those at the center of the discharge electrodes. Bleecker et al.[12] carried out the simulation of the SiH_4 plasma (50 MHz) at 40 Pa using a one-dimensional fluid model and examined a dusty plasma by calculating higher-order silanes, where Perrin's rate constant was used for Eq. (1.2). In their case, many negative ions were generated, $n_e \ll {SiH_3}^-$ density, and the SiH_3 density at the center of two discharge electrodes was around $3 \times 10^{18}\,m^{-3}$, which is one order of magnitude lower than this work.

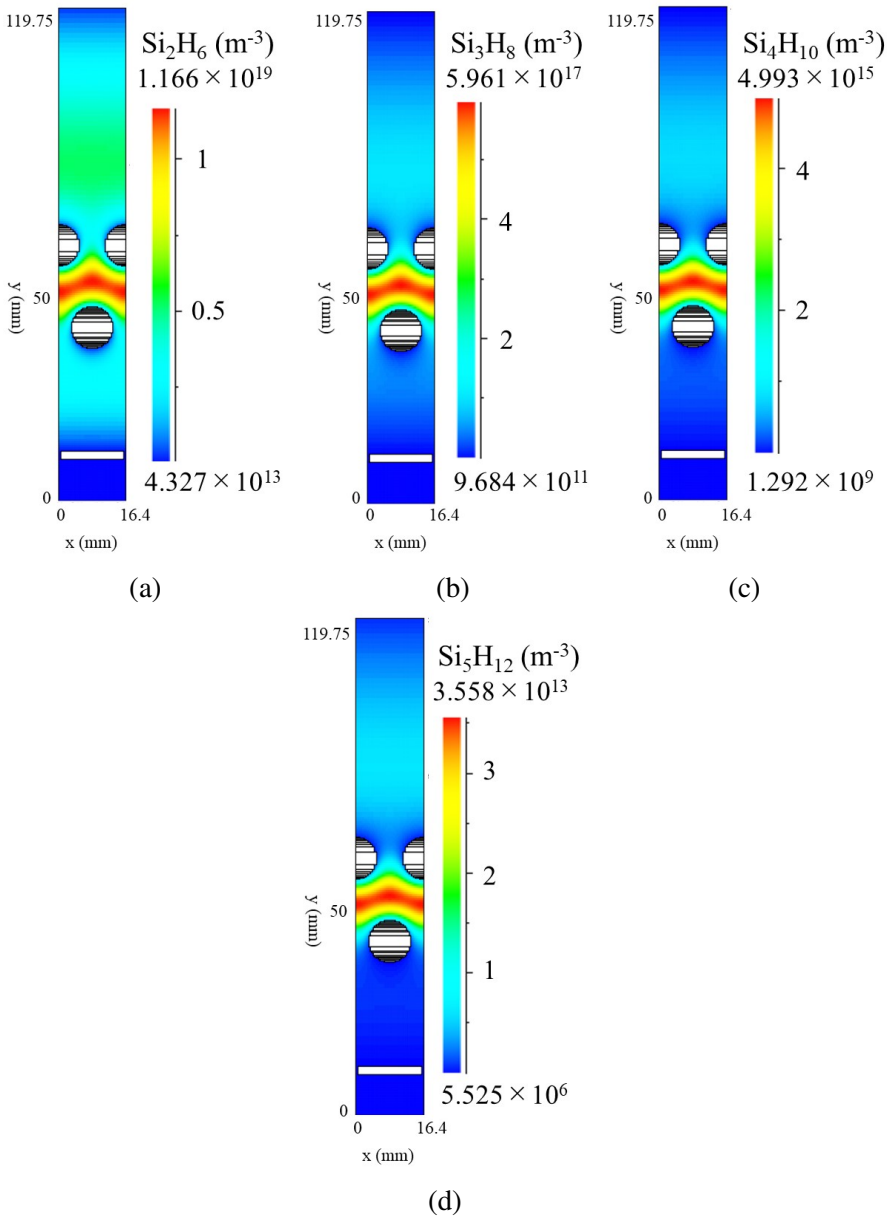

Figure 3.21: Spatial profiles of higher-order molecules: (a) Si_2H_6, (b) Si_3H_8, (c) Si_4H_{10}, and (d) Si_5H_{12} densities, where the pressure is 13.3 Pa.

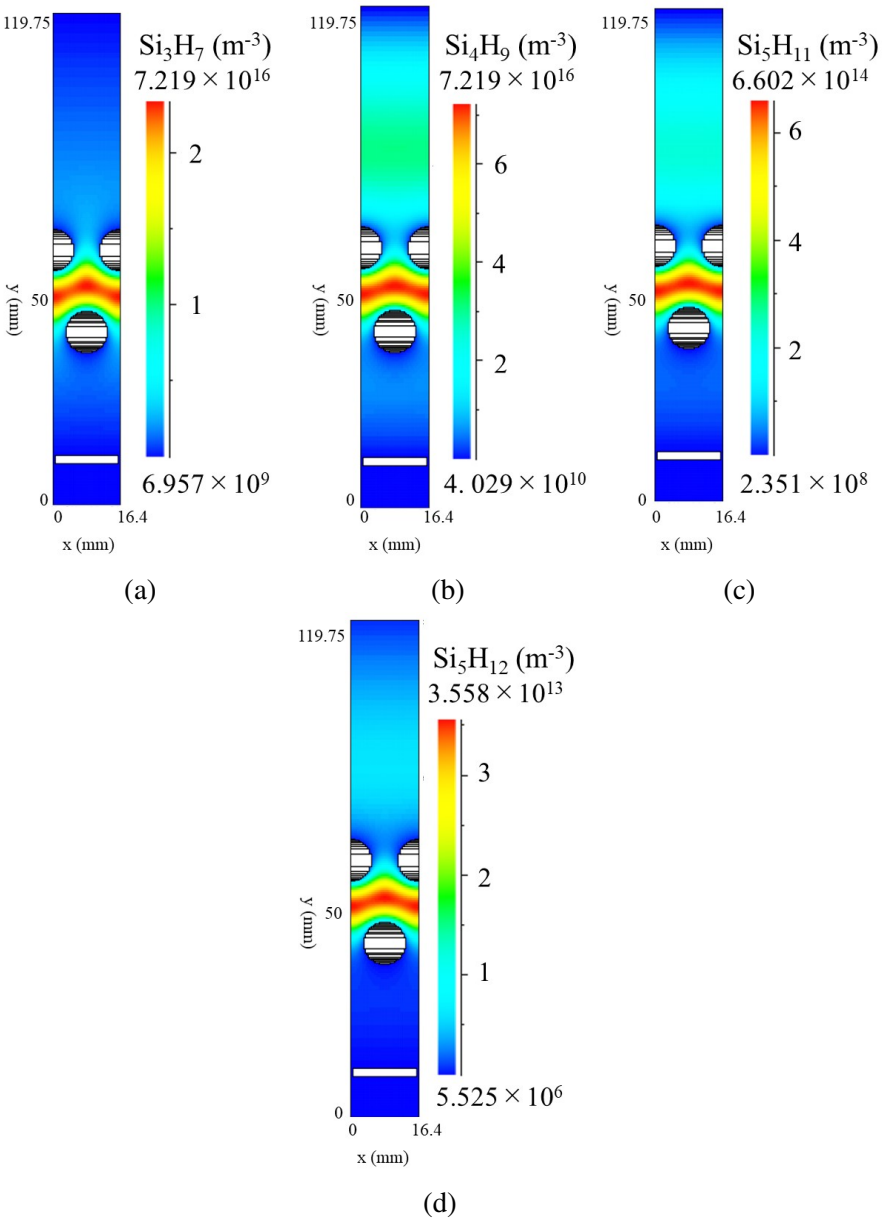

Figure 3.22: Spatial profiles of higher-order molecules: (a) Si_3H_7, (b) Si_4H_9, (c) Si_5H_{11}, and (d) Si_5H_{12} densities, where the pressure is 13.3 Pa.

However, the density ratio SiH_3/SiH_2 is equal to 100 at the center. On the other hand, the densities of Si_4H_{10} and Si_5H_{12} at the center were on the order of 10^{19} m^{-3}, indicating that such densities are few orders of magnitude higher than this work. In addition, the

radical densities of Si_3H_7, Si_4H_9, and Si_5H_{11} shown in Fig. (3.22) were few orders of magnitude lower than Bleecker et al.'s result. Experimentally, Nunomura and Kondo [50] studied gas phase kinetics of a VHF SiH_4/H_2 plasma using a quadrupole mass analyzer and estimated the molecular densities that were much higher than in this work. In their case, nanoparticles were formed. Therefore, it is concluded that high-quality amorphous silicon will be fabricated even between discharge electrodes under these simulation conditions.

Here, to examine the effect of the rate constant for Eq. (1.2) on the SiH_3 radical density, the 2D maps are calculated for the plasma parameters, radicals, and molecules using Perrin et al.'s rate constant for Eq. (1.2). The spatial distributions of SiH_3, SiH_2, and SiH densities at x = 0 are shown in Fig. (3.23), where the simulation conditions are the same as those for NIST-PML. Such densities at y = 57-67 mm are 0. Fig. (3.23) demonstrates that the SiH_3 and SiH_2 densities are equal to 4.1×10^{19} m^{-3} and 6.6×10^{17} m^{-3} inside the discharge electrodes, respectively; thus, the density ratio SiH_3/SiH_2 is equal to 63, which is higher than the result in Fig. (3.20). Thus, including Kushner's result [31], it seems that a high rate constant for Eq. (1.2) provides a high SiH_3 density that must be confirmed for different conditions such as different pressures and discharge gap distances.

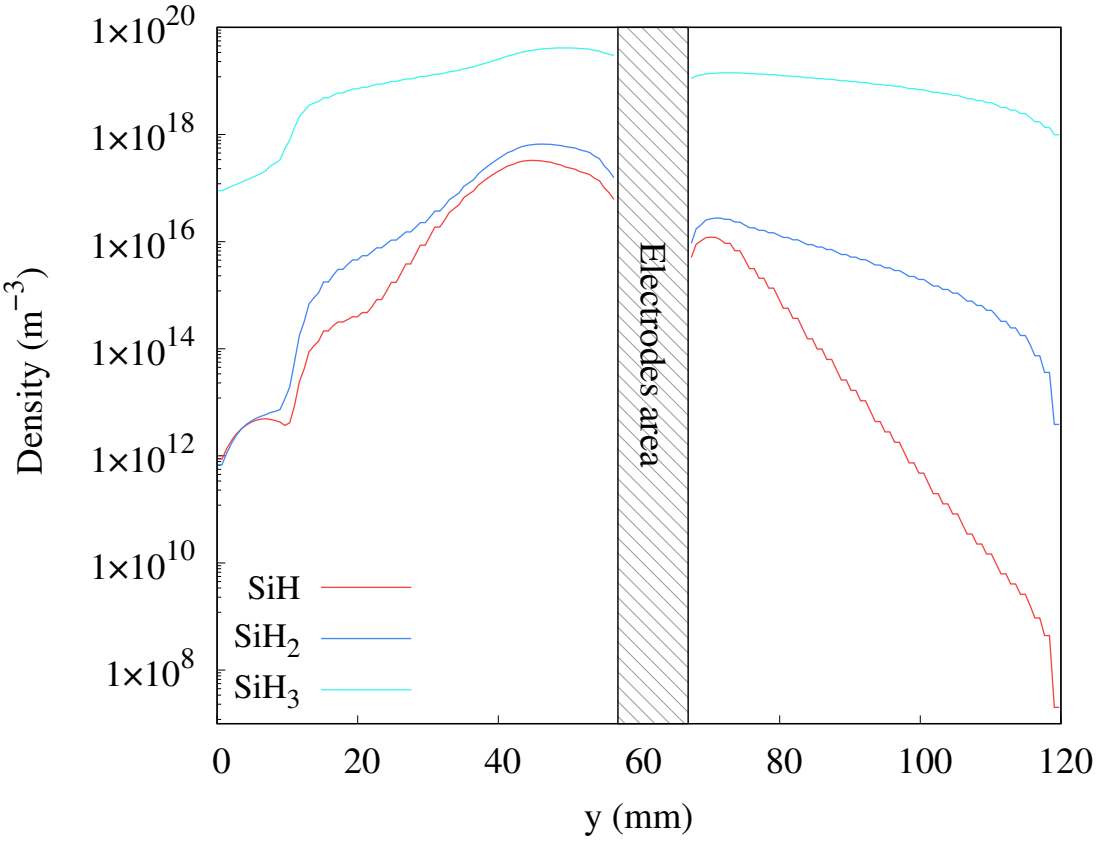

Figure 3.23: Spatial distributions of SiH, SiH_2, and SiH_3 densities at x = 0 at a pressure of 13.3 Pa, where Perrin et al.'s rate constant was used. No plasma is produced at y = 57-67 mm corresponding to the discharge electrodes.

In addition, the higher-order molecule and radical densities are almost the same as the results shown in Fig. (3.21) and (3.22), indicating that the rate constant for Eq. (1.2) slightly affects the generation of higher-order silanes. This is consistent with the fact that SiH_3 radicals are not reactive. Thus, it can be concluded that the density ratio SiH_3/SiH_2 is one of the measures of film quality, however, the information about higher-order silanes is also necessary for judging the film quality.

Kushner [31] explains that electron impact dissociation predominates SiH_3 radical

production near discharge electrodes and that hydrogen abstraction is more predominant near the center of the reactor. Rehman et al.[3] reported that hydrogen abstraction is predominant in SiH_3 radical generation at pressures higher than 100 Pa. Recently, Hayashi et al. [19] have reported that hydrogen abstraction cannot be ignored. As already described, the results from this work indicate that both electron impact dissociation and hydrogen abstraction occur between the discharge electrodes and both reactions contribute to their generation. Then, as is pointed out, the SiH_3 radicals generated between the discharge electrodes diffuse with collisions toward the substrate.

The effect of various parameters on the deposition rate has been studied by some researchers [23, 31, 38]. In particular, the discharge gap distance d is an important parameter in the CCP [8], and spatial profiles of SiH_4 plasma parameters and radicals depend on d. Mataras [38] reported the optimum gap distance d_0 at which the deposition rate was maximum at a constant pressure; d_0 = 15 mm at a frequency of 50 MHz and a pressure of 66.7 Pa. Kushner [31] calculated the spatial profiles of SiH_3 for different d values at a frequency of 13.56 MHz and found that, when d increased, the SiH_3 density decreased. In addition, when d decreases, T_e tends to increase in the VHF plasma [25]. In this simulation, d = 10 mm, which is slightly short, but a preferable VHF plasma was obtained; $n_e = 1 \times 10^{16}\,\mathrm{m}^{-3}$ and T_e = 2 eV at 13.3 Pa. Thus, although the d dependence of the plasma characteristics was not examined, it may be close to the optimum conditions for the deposition.

The determination of the electron energy distribution function (EEDF) is important in CCP simulations. The EEDF deviates from a Maxwellian distribution in a high energy region; thus, this deviation affects electron impact ionization [18]. In this study, it was assumed that electrons had a Maxwellian distribution because it was focused on the characteristics of the triode plasma source that can fabricate high-quality amorphous silicon with a high deposition rate. As is well known, stochastic heating [34] occurs in the CCP at low pressures and, as a result, electrons have a bi-Maxwellian velocity distribution function, which might change plasma processing. A simulation considering the electron velocity distribution function will be a future study.

As is well known, sticking coefficients of radicals play an important role in their density distributions and film growth. As seen in Fig. (3.21), the Si_2H_6, Si_3H_8, Si_4H_{10}, and Si_5H_{12} densities decrease near the rod electrodes, while some researchers [43, 77] reported that they were uniform. Here, it was assumed that the sticking coefficients of higher-order silanes were 1.0; thus, the decreases in higher-order silanes densities near the rod electrodes are considered to be due to higher sticking coefficients. However, there might be another reason for such decreases. In this simulation, for simplicity, the continuity equation was not solved for neutral particles. Instead, it is assumed that the pressure is constant in the chamber, that is, the gas inlet and pumping are not taken in account, which may change the density profiles of higher-order silanes near the rod electrodes. In fact,

uniform density profiles of higher-order silanes were obtained in the case of a multi-hollow plasma, where in the simulation the continuity equation was solved for neutral particles and the sticking coefficient of 1.0 was used. Thus, it is an interesting subject to examine the density profiles of higher-order silanes for different sticking coefficients together with solving the continuity equation for neutral particles. That will be a subject of future study.

To analyze the effect of pressure on the SiH_4 plasma properties near the substrate, a position of 3 mm from the substrate was selected in the middle of the horizontal axis of the simulation profile, as shown in Fig. (3.15). The pressure dependence of the higher-order silanes densities is demonstrated on the example of Si_5H_{12}. Fig. (3.25) shows the density profile of Si_5H_{12} as a function of pressure where it peaks around 26.7 Pa. At the same time, the electron density has a minimum value at 26.7 Pa as can be seen in Fig. (3.24).

At all studied pressures the results show very low electron densities n_e in the range of 10^{13} m^{-3} near the substrate. The densities of SiH_3 and SiH_2 shown in Fig. (3.26) and Fig. (3.27) are steadily decreasing with increasing the pressures. This behavior is expected because SiH_3 and SiH_2 radicals only diffuse to the substrate from the production area between the electrodes. The SiH_3 density dependence on the pressure is for the most part linear, while the density of SiH_2 has more exponential-like dependence. The density of SiH_2 at the pressure of 66.7 Pa drops to 3.6×10^{11} m^{-3}. That is suggesting an additional process of depletion of SiH_2 in dependence on the pressure such as the creation of higher

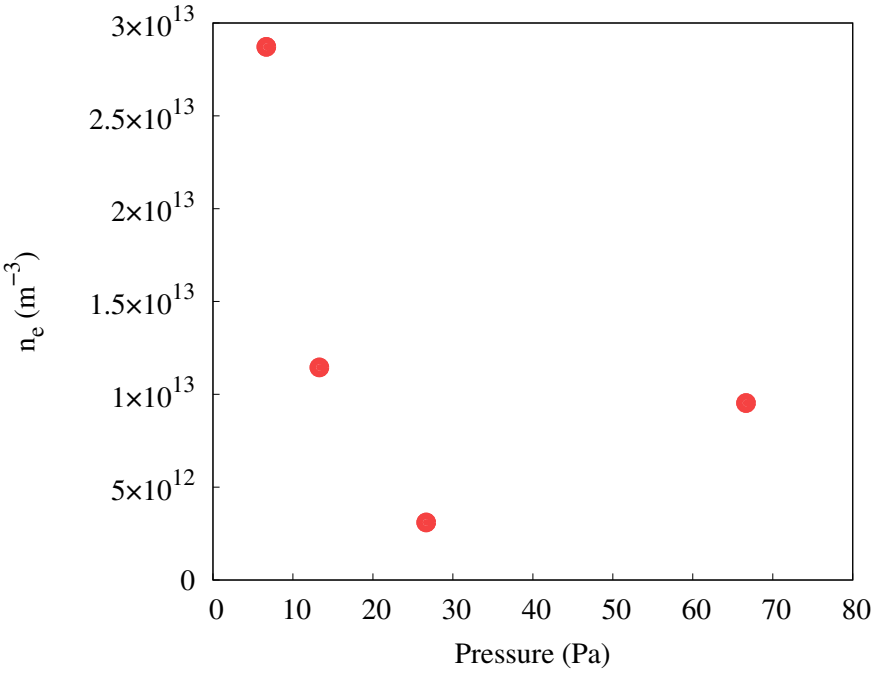

Figure 3.24: Pressure dependence of n_e at 3mm from the substrate.

order silanes. On the other hand, the density of Si_5H_{12} near the substrate is as low as $10^{12}\,m^{-3}$ at all the selected pressures. This suggests there are almost no dust particles near the substrate. However, to fully understand the plasma characteristics dependence on the pressures, further research on the frequency, amplitude, and pressure settings will be necessary.

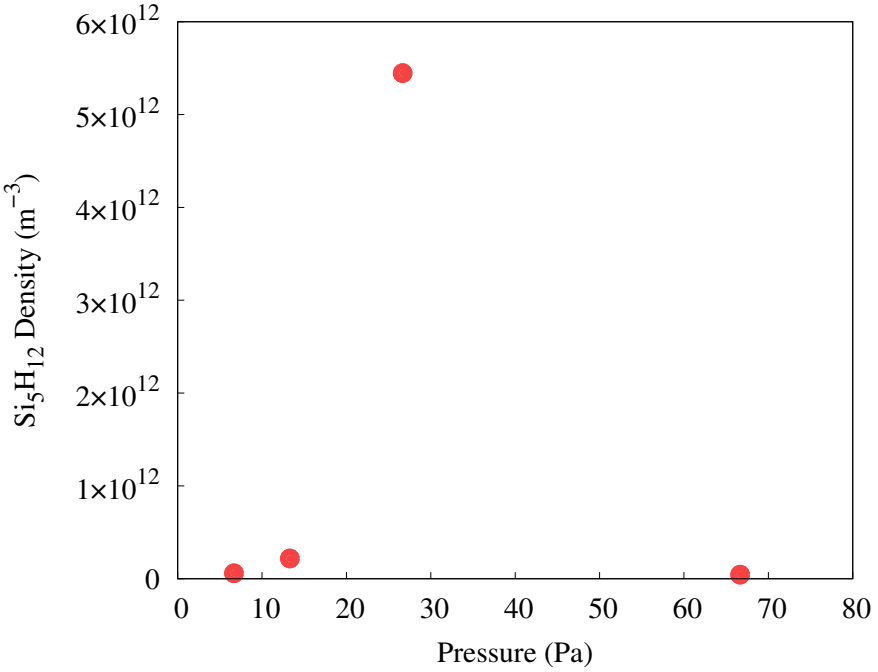

Figure 3.25: Pressure dependence of Si_5H_{12} density at 3mm from the substrate.

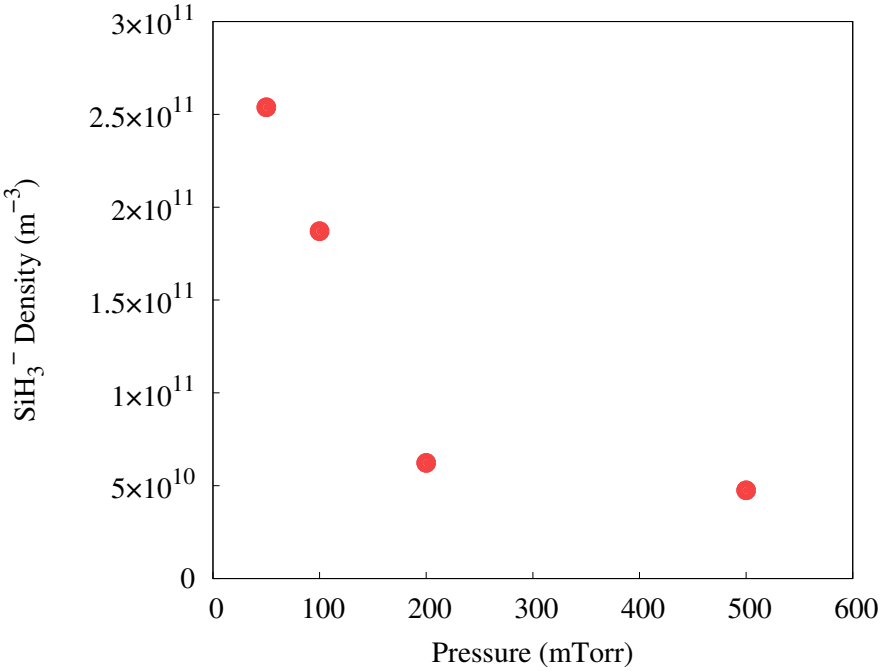

Figure 3.26: Pressure dependence of SiH_3 density at 3mm from the substrate.

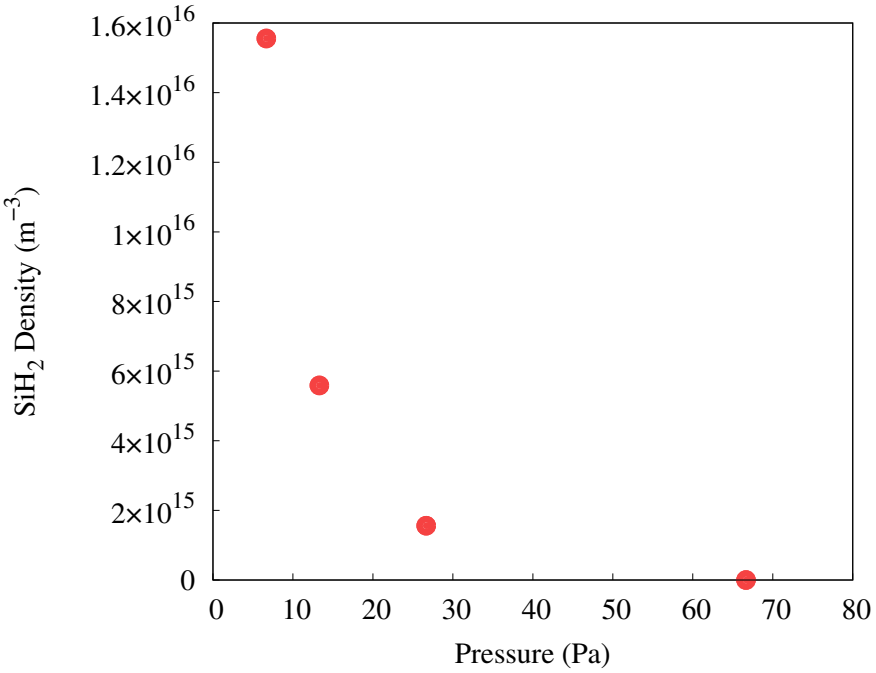

Figure 3.27: Pressure dependence of SiH_2 density at 3mm from the substrate.

3.2.4 Conclusions

In this work the characteristics of a triode VHF SiH_4 plasma (frequency, 60 MHz) using a fluid model were examined, where the plasma was produced by multi-rod (staggered) electrodes, and the following results were found:

(1) A typical VHF plasma with a high n_e ($\sim 1 \times 10^{16}$ m^{-3}) and a low T_e ($\sim$2 eV) is produced between discharge electrodes, while n_e near the substrate is very low. Dominant ions are SiH_3^+.

(2) A preferable characteristic of a high SiH_3 density near the substrate is found. The density ratio SiH_3/SiH_2 is determined to be 25 and 100 near the center and substrate, respectively.

(3) The densities of higher-order silanes that contribute to dust formation are five to six orders of magnitude lower than the SiH_3 density and have similar spatial profiles, so the quality of amorphous silicon fabricated with the multi-rod electrodes will be expected to be high.

(4) The rate constant of $SiH_3 + SiH_3 \longrightarrow SiH_2 + SiH_4$ affects the SiH_3 density.

In Chapter 3, two types of VHF CCPs were simulated using the PHM. It was found that the multi-rod electrodes can provide high-quality amorphous silicon with high deposition rates, while the multi-hollow geometry electrodes generates many dust particles. In addition, it is for the first time that the characteristics of the triode VHF-CCPs including higher-order silanes such as Si_5H_{12} were studied by simulations. Physical explanations about such characteristics will be a future subject.

Chapter 4

PIC simulation of VHF Ar plasma

4.1 Introduction

There has been a current tendency that a power generator frequency is increased to obtain high rates of etching. Recently, VHF plasma sources at excitation frequencies of 100-150 MHz have become popular in etching [13, 76]. In fact, when the frequency is increased, the electron density increases, leading to a high etching rate. However, as is well known, electromagnetic effects such as standing wave and skin effects [33] arise at high frequencies, and as a result, the electron density distribution along the discharge electrodes becomes nonuniform [20]. Overzet and Hopkins [55] observed the off-axis radial peak in electron density in the Ar plasma even at a frequency of 13.56 MHz, which was explained by the fluid model simulation [37]. On the other hand, Yamazawa [75] investigated the effect of harmonics on the electron density and reported a center-peaked electron density profile that was caused by a nonlinear electron resonance heating. In addition, Sawada et

al. [59] observed that the electron density in the VHF Ar plasma at a frequency of 60 MHz had a center-peaked profile. Thus, the study of a spatial distribution of VHF Ar CCPs is an important subject in etching and has been examined by many researchers [8, 59, 76]. The Langmuir probe method is a simple and powerful diagnostic tool in a low temperature plasma and is mostly used [55] to measure the plasma parameters such as the density and temperature of electrons. However, there is possibility that a Langmuir probe disturbs VHF discharges; spatial distributions of the plasma parameters are deformed by introducing the probe. Therefore, in order to develop a new VHF CCP source for etching, in this thesis the characteristics of VHF Ar plasmas were studied by simulation. As is well known, there are three kinds of simulation models to examine the behaviors of a low temperature plasma, that is, fluid model, hybrid model, and particle-in-cell (PIC) model. The fluid model is useful at high pressures while the PIC model is effective at low pressures. The properties of CCPs have been extensively investigated using a two-dimensional (2D) hybrid model [8, 76]. Yang and Kushner [76] explained a shift in the peak electron density toward the center of the plasma source as the power source frequency increased. Bera et al. [4] tried to control plasma uniformity using two frequency power sources at a combination frequency of 60 and 180 MHz and compared with the simulation by a 2D fluid model including Maxwell equations. They also calculated the electron density profile by a one-dimensional (1D) PIC simulation, where electromagnetic effects were not considered, and found that the electron density became maximum at the center with large contribution of the 180 MHz power source to plasma production and the electron energy distribution

deviated from Maxwellian one. Generally, an electron energy distribution function in VHF plasmas is not Maxwellian at low pressure. In fact, Godyak and Piejak [16] observed that electrons had a bi-Maxwellian distribution. Thus, it is necessary to incorporate a kinetic description of electrons and ions in the simulation for understanding self consistently the plasma characteristics. The best calculation is to use the PIC/Monte Carlo (MC) method [71] because the fundamental equations can be employed without much approximation. In this chapter two dimensional (2D) profiles of the plasma parameters are calculated using a 2D Particle-In-Cell with Monte Carlo Collision Module (PIC-MCCM) of PEGASUS Software [56], where electromagnetic effects are not included, that is, it is assumed that electrostatic fields are dominant in the VHF discharge.

4.2 Description of simulation model

The PIC/MC method is based on a kinetic description of charge particle motions in phase space. Charged particles move in the self-consistent electric field that is obtained by solving the Poisson equation. The Monte Carlo method is used to calculate collisions including excitation and ionization. The PIC method has been described in detail by Birdsall [6], Turner [69], and Verboncoeur [71]. In the PIC-MCCM of PEGASUS Software, electrons and ions are modeled as a large number of representative particles that are referred to as simulated particles (superparticles). A motion of the individual superparticle is subject to the Newton's law in the electric field. Various kinds of collisions are also taken into account using Monte Carlo collision method. Macroscopic quantities

of the electron and ion densities, mean energy, particle flux are obtained by statistical calculations using velocities and positions of all the superparticles. Here, it is assumed that there are two kinds of charged particles in the plasma for saving the computation time: electrons and Ar^+ ions. Fig. (4.1) is a schematic of the CCP source simulated in this work (380 x 45 mm^2), where a Cartesian coordinate is used and a symmetric plane at the center between two discharge electrodes is assumed. A power source frequency was 100 MHz, where external circuit was not included. The gas used was Ar and the pressure varied from 20 to 100 mTorr. The initial conditions for superparticles were: the density = 3×10^5 m^{-3} for electrons (10^{15} m^{-3}) and ions (10^{15} m^{-3}).

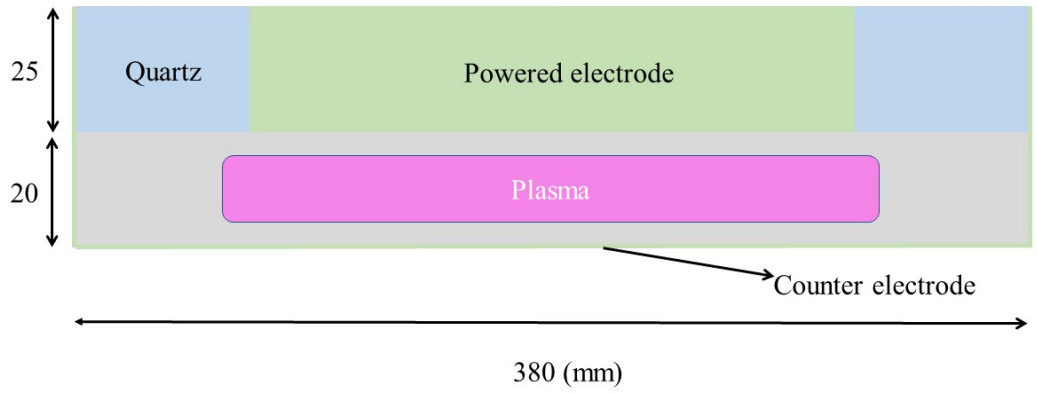

Figure 4.1: Schematic cross section of the VHF CCP source.

4.3 Results and discussion

Since a VHF CCP source provides a high electron density plasma with a low electron temperature, it has been popular for etching. On the other hand, the self-bias voltage formed on the power electrode that is indispensable for etching is much lower than that at a power source frequency of 13.56 MHz. Therefore, recently dual-frequency power sources have been employed for etching. In this study, the simulations at a single power source frequency was performed as a first step for developing a large-area VHF CCP source. At first, the time history of the self-bias voltage V_{dc} at a pressure of 40 mTorr was calculated. Fig. (4.2) shows that V_{dc} saturates to – 3.3 V that is very low for etching, as expected.

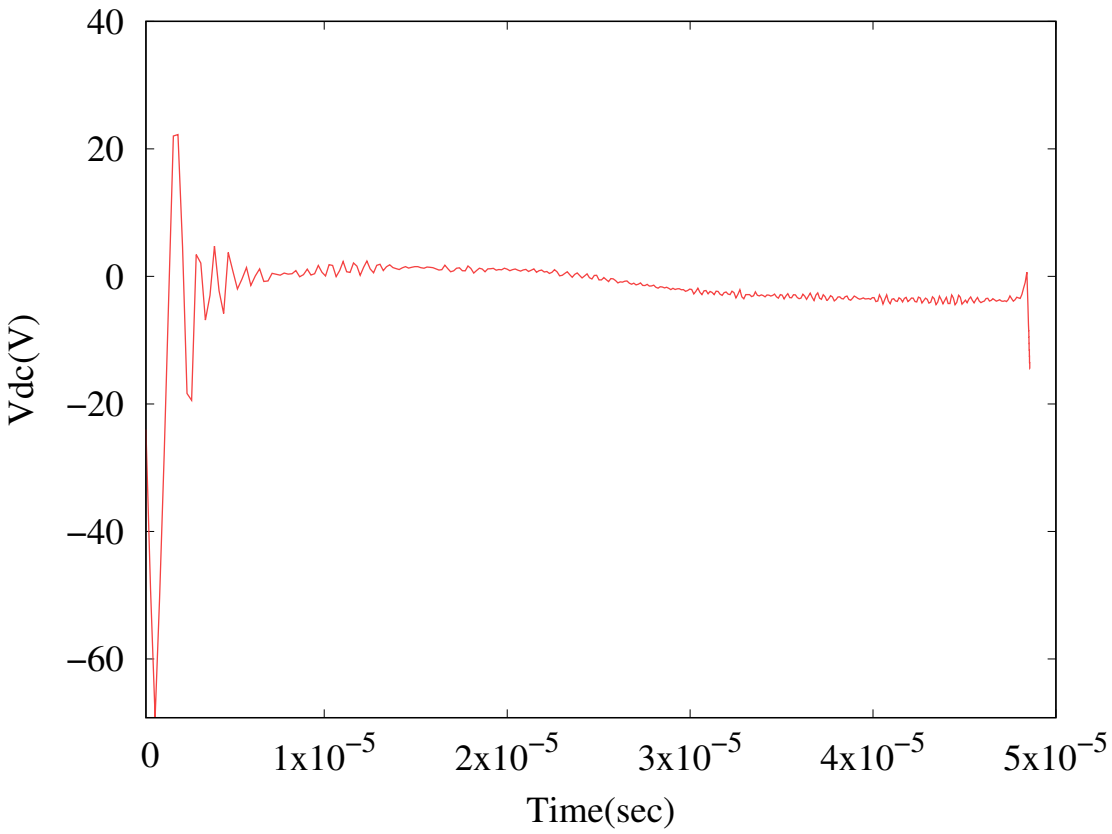

Figure 4.2: Schematic of the VHF CCP source Time history of the self-bias voltage, Vdc, on the powered electrode at a pressure of 40 mTorr, where the amplitude is 30 V.

A two-dimensional (2D) map of the plasma parameters was calculated. The results at 40 mTorr are shown in Fig. (4.3) to (4.5), where the amplitude is 30 V. Fig. (4.3) shows that the electron density n_e amounts to 3.6×10^{16} m^{-3}. Note that n_e peaks at x = 75 and 190 mm, that is, the electron density peaks both near the edge of the discharge electrodes and the chamber center. Bera et al. [5] simulated a VHF-CCP at a frequency of 180 MHz using the 2D fluid model coupled with Maxwell equations and found the two-peak profile at a narrow gap of 17.8 mm at a pressure of 100 mTorr. They also reported that as the gap distance was increased, the electron density profile became to a center-peaked profile. In

addition, Sawada et al. [59] carried out the experiments on a VHF-CCP at power source frequencies of 60 and 106 MHz and compared with the simulations taking into account of Maxwell equations. They pointed out that higher harmonics of a power source frequency affected the electron density profile. As already described, here the Maxwell equations are not solved, so it can be concluded that the two-peak profile may be due to other effects.

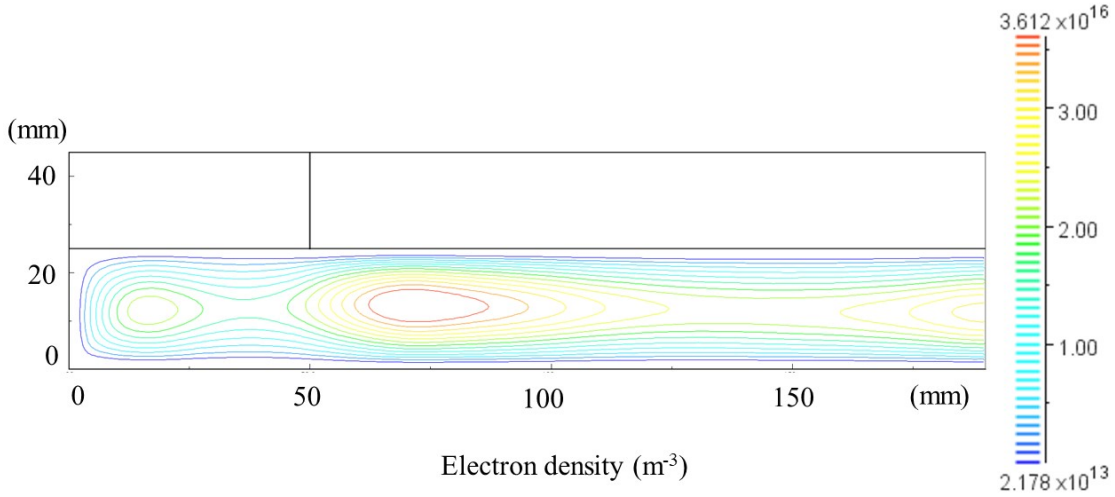

Figure 4.3: 2D map of the electron density n_e at a pressure of 40 mTorr, where the amplitude is 30 V.

Fig. (4.4) shows that the electron temperature T_e also has a peak value at x = 75 and 190 mm and T_e is around 2 eV. Note that T_e near the discharge electrodes is around 3 eV that is a little higher than T_e at the center. The CCP is produced by electron impact ionization, so T_e near the electrodes becomes higher. In this study, the power source frequency is 100 MHz, so VHF effect will be higher, leading to a low electron temperature. There have

been many reports on spatial distributions of the electron density of VHF-CCPs, that is, researchers have mostly focused on the electron density profile. Spatial distributions of the electron temperature, especially those near the discharge electrodes, are also important because it is closely related to the sheath formation on the substrate.

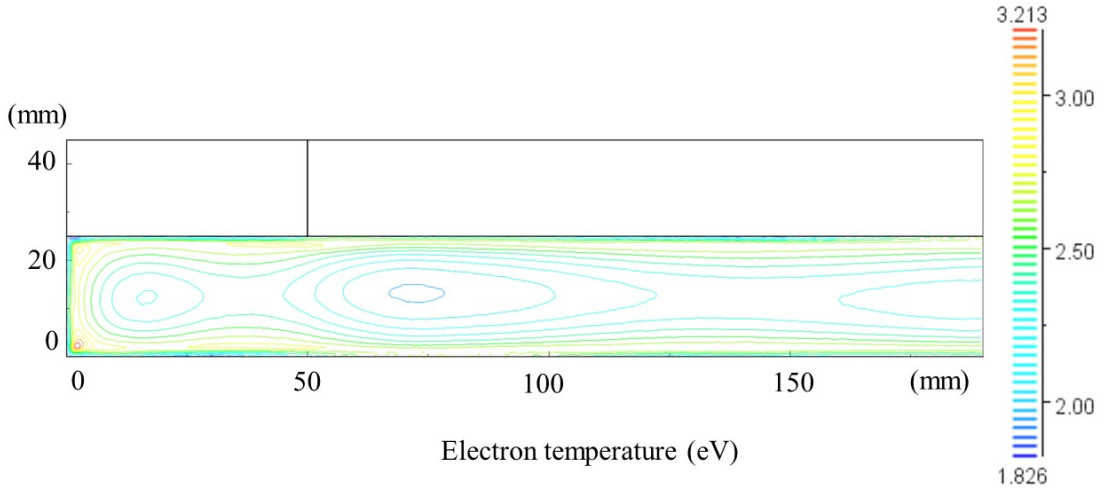

Figure 4.4: 2D map of the electron temperature T_e at a pressure of 40 mTorr, where the amplitude is 30 V.

Fig. (4.5) shows that the plasma potential V_s is around 32 V and fairy uniform over the discharge electrodes. Looking carefully at V_s close to the discharge electrodes, it is not uniform, and the thickness of the sheath formed on the grounded electrode is not uniform, suggesting that it will not easy to control energy distribution functions of charged particles by dual-frequency technology [76].

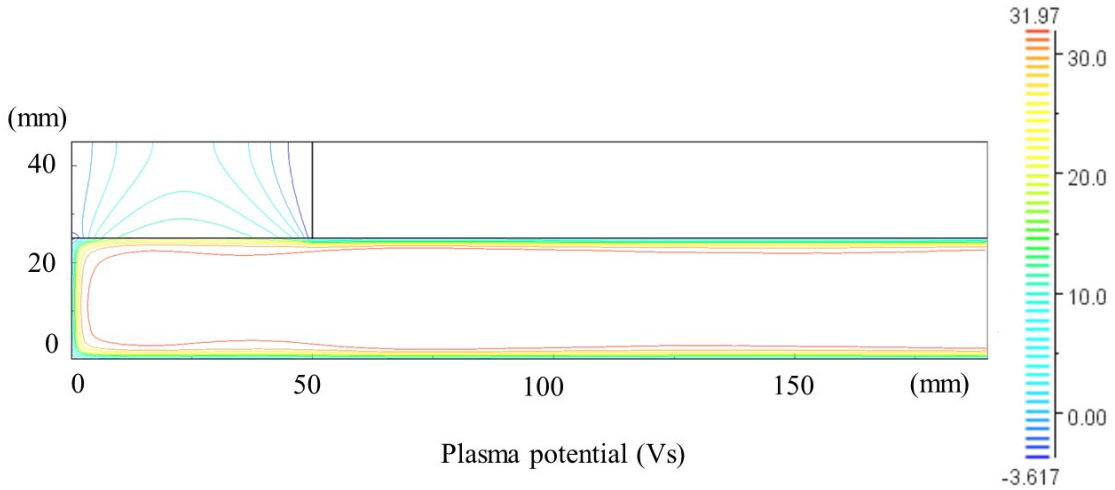

Figure 4.5: 2D map of the plasma potential V_s at a pressure of 40 mTorr, where the amplitude is 30 V.

Energy distribution functions of charged particles play an important role in etching as well as plasma production. The energy distribution functions of electrons (EEDF) and ions (IEDF) were calculated at different monitoring positions denoted by P_i. As seen in Fig. (4.6)(a), electrons have a Maxwellian distribution function in the low energy region. In fact, it has been confirmed that semi-log plots of the EEDFs fit to a straight line in the energy region of (0-15) eV and high energetic electrons are truncated, that is, the obtained EEDF looks a Druyvesteyn-like distribution function [21]. Experimentally, Godyak and Piejak [16] observed the bi-Maxwellian and Druyvesteyn distribution functions at low and high pressures, respectively, at a frequency of 13.56 MHz. Abdel-Fattah and Sugai [1] also measured EEDFs for different power source frequencies ranging from 13.56 to 60 MHz and reported that the EEDFs became a Druyvesteyn distribution function below 30

MHz and a bi-Maxwellian distribution function above 30 MHz. In this simulation, the VHF plasma was generated at 40 mTorr at 100 MHz, but the bi-Maxwellian distribution function was not obtained, so it can be concluded that the effect of stochastic heating [33] on the plasma generation is negligible small. Fig. (4.6) also indicates that the electron density is lower and electron temperature is higher at a monitoring position of P_1 (inside the ion sheath) which agrees with the results of Fig. (4.3) and (4.4). On the other hand, ions were cold except at P_1 where ions are accelerated by the sheath potential.

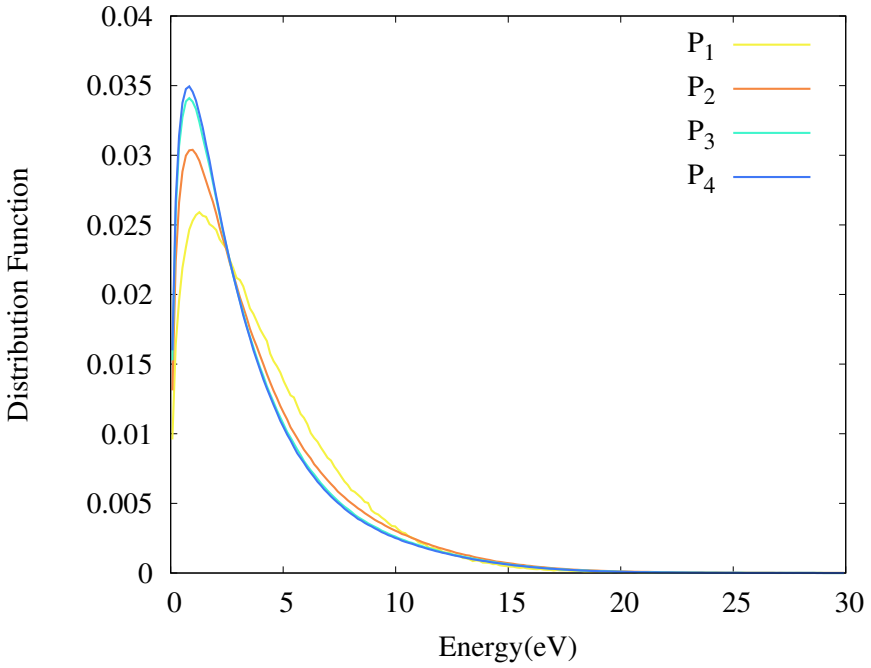

(a)

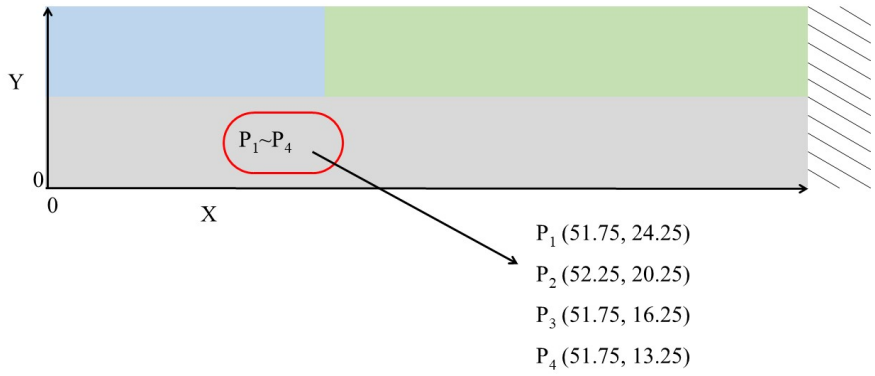

(b)

Figure 4.6: Energy distributions: (a) EEDFs for different monitoring positions at a pressure of 40 mTorr, where the amplitude is 30 V and (b) the monitoring positions of electron energy distributions.

As aforementioned, a two-peak profile of the electron density has been found in the VHF electrostatic discharge by the PIC simulation. As is well known, the PIC simulation is

more accurate than the fluid model simulation because of fewer assumptions for modeling. To understand the two-peak profile, it is necessary to examine the parametric dependences of the 2D map such as the pressure and gap dependences. This will be discussed in future.

4.4 Conclusions

The characteristics of the VHF Ar plasma (100 MHz) were calculated at a pressure of 40 mTorr using the PIC-MCCM of PEGASUS Software, where it was assumed that the plasma is produced by electrostatic fields. The following results were found:

(1) The self-bias voltage is as low as a few volts.

(2) The 2D maps of the electron density and electron temperature show that they peak both near the center and the edge of the discharge electrodes, while the plasma potential is fairly uniform.

(3) The electron energy distribution function is similar to the Druyvesteyn-like one.

In summary, it is concluded that the above-mentioned results will be useful for designing a VHF plasma source for large-area etching. The simulation using the dual-frequency power sources will be a subject of future study.

Chapter 5

Conclusions

5.1 Conclusions

In Chapter 2 the mechanism of VHF plasma was explained. The function of simulation tool, plasma hybrid module (PHM) of PEGASUS Software was described. The fluid equations used in PHM consist of the continuity equation, equation of motions, and energy balance equation which are described in Appendix 3. The PHM performs the simulations combining Poisson's equation module (PEM) to calculate electric fields, the electron Monte Carlo simulation module (EMCSM) to obtain electron energy distribution functions, and the drift-diffusion equation module (DDEM). The PEM calculates an electric field with Poisson's equation by the semi-implicit method.

In the beginning of Chapter 3 the VHF SiH_4/H_2 plasma with the multi-hollow geometry was simulated and the interesting results were found. First, a typical VHF plasma

of high n_e and low T_e is produced between two discharge electrodes, anode and rods electrodes, while n_e near the substrate is much lower than that between the discharge electrodes. Second, the rate constant of $SiH_3 + SiH_3 \longrightarrow SiH_2 + SiH_4$ affects generation of SiH_3 radicals. Third, preferable characteristics of a high SiH_3 density and a low electron temperature near the substrate are found. Many negative ions exist. Fourth, the ratio of SiH_3/SiH_2 and SiH_3/SiH near the substrate is very high. Last, the Si_5H_{12} density near the substrate is comparable to the SiH_3 density, suggesting dust formation. The above mentioned results indicate the multi-hollow geometry plasma source may not be suitable for the fabrication of amorphous silicon. Simulations at higher pressures will be a future subject. In the second part of the Chapter 3, the triode VHF SiH_4 plasma (frequency, 60 MHz) was simulated using a fluid model, where the plasma was produced by multi-rod (staggered) electrodes. The obtained results are: First, a typical VHF plasma with a high n_e ($\sim 1 \times 10^{16}\,m^{-3}$) and a low T_e ($\sim 2\,eV$) is produced between discharge electrodes, while n_e near the substrate is very low. Dominant ions are SiH_3^+. Second, a preferable characteristic of a high SiH_3 density near the substrate is found. The density ratio SiH_3/SiH_2 is determined to be 25 and 100 near the center and substrate, respectively. Third, the densities of higher-order silanes that contribute to dust formation are five to six orders of magnitude lower than the SiH_3 density and have similar spatial profiles. Fourth, the rate constant of $SiH_3 + SiH_3 \longrightarrow SiH_2 + SiH_4$ affects the SiH_3 density. Last, the Si_5H_{12} density has a maximum at a certain pressure.

In Chapter 4 the characteristics of the VHF Ar plasma (100 MHz) at a pressure of 40 mTorr was studied using the PIC-MCCM of PEGASUS Software, where it was assumed that the plasma is produced by electrostatic fields. The following results were found: First, the self-bias voltage is as low as a few volts. Second, The 2D maps of the electron density and electron temperature show that they peak both near the center and the edge of the discharge electrodes, while the plasma potential is fairly uniform. Third, the electron energy distribution function is similar to the Druyvesteyn-like one. It can be concluded that the above-mentioned results will be useful for designing a VHF plasma source for large-area etching. The simulation using the dual-frequency power sources will subject of a future work.

5.2 Outlook of future work

It has been shown that the multi-rod electrodes can provide high quality amorphous silicon with high deposition rates. Amorphous silicon thin film solar cells have an advantage that they will be suitable in tropical counties, so further development will be needed for the cost reduction of amorphous silicon thin film solar cells. Recently, the conversion efficiency of crystal silicon solar cells is remarkably increasing by introducing a new a-Si/c-Si heterojunction structure called HIT (heterojunction with intrinsic thin layer) [65].

The HIT structure features a very thin intrinsic a-Si layer inserted between a doped a-Si layer and a c-Si substrate. The conversion efficiency of 21.5 % with a size 100 x 3 cm^2

has been achieved. Solar cell industries require higher quality amorphous silicon films for HIT solar cells. The author believes that obtained simulation results will contribute to an increase in the conversion efficiency of HIT solar cells.

In addition, SiH_4 CCP based deposition such SiN_xH_y (Hydrogenated silicon nitride) films are important for the fabrication of ultra/very-large-scale-integrated circuits. Therefore, the VHF SiH_4 plasma using multi-rod electrodes will be useful for designing a VHF plasma source for the fabrication of semiconductors and will attract more development in the future.

One of key issues in etching is plasma uniformity and complicated ideas have been proposed to explain non-uniformity in electron density. This two-dimensional PIC simulation showed that an electrostatic discharge plasma has two peaks on the electron density profile. In actual etching devices, at least two power sources with different frequencies have been used, so called dual-frequency technology. Dual-frequency technology might solve this problem, where the control of an ion energy distribution is very important. In addition, as discussed by many researchers, the structure of VHF-CCP source, especially the edge of the plasma source affects uniformity [59], so a study to optimize the VHF-CCP source for etching will be necessary.

References

[1] E. Abdel-Fattah and H. Sugai. *Applied Physics Letters*, 83(8):1533–1535, 2003.

[2] L. Alagappan, R. Orans, and C.K. Woo. *Energy Policy*, 39(9):5099–5104, sep 2011.

[3] Aman-Ur-Rehman, H. C. Kwon, W. T. Park, and J. K. Lee. *Physics of Plasmas*, 18(9):0–12, 2011.

[4] Kallol Bera, Shahid Rauf, Kartik Ramaswamy, and Ken Collins. *Journal of Applied Physics*, 106(3):033301, aug 2009.

[5] Kallol Bera, Shahid Rauf, Kartik Ramaswamy, and Ken Collins. *Journal of Vacuum Science & Technology A: Vacuum, Surfaces, and Films*, 27(4):706–711, jul 2009.

[6] C. K. Birdsall. *IEEE Transactions on Plasma Science*, 19(2):65–85, 1991.

[7] Kuan-chen Chen, Kohei Ogiwara, Kuo-feng Chiu, Li-wen Su, Kiichiro Uchino, and Yoshinobu Kawai. *Japanese Journal of Applied Physics*, 55(7S2):07LD01, jul 2016.

[8] Kuan-Chen K.-C. Chen, K.-F. Kuo-Feng Chiu, Kohei Ogiwara, Li-Wen Su, Kiichiro Uchino, and Yoshinobu Kawai. *Japanese Journal of Applied Physics*, 56(1S):01AC05, jan 2017.

[9] Weiting CHEN, Kohei OGIWARA, Koichiro KOGE, Kentaro TOMITA, Kiichiro UCHINO, and Yoshinobu KAWAI. *Plasma and Fusion Research*, 8:1306114–1306114, 2013.

[10] Zhigang Chen, Shahid Rauf, and Ken Collins. *Journal of Applied Physics*, 108(7), 2010.

[11] Kathleen De Bleecker, Annemie Bogaerts, Renaat Gijbels, and Wim Goedheer. *Physical Review E*, 69(5):056409, 2004.

[12] Kathleen De Bleecker, Annemie Bogaerts, Wim Goedheer, and Renaat Gijbels. *IEEE Transactions on Plasma Science*, 32(2 II):691–698, 2004.

[13] Vincent M. Donnelly and Avinoam Kornblit. *Journal of Vacuum Science & Technology A: Vacuum, Surfaces, and Films*, 31(5):050825, sep 2013.

[14] European Commission. 2018, https://ec.europa.eu/energy/en/topics/renewable-energy.

[15] Federal Agency Use of Renewable Electric Energy. 2016, https://www.energy.gov/eere/femp/federal-agency-use-renewable-electric-energy.

[16] V. A. Godyak and R. B. Piejak. *Physical Review Letters*, 65(8):996–999, 1990.

[17] Y. Hashimoto, S. Toko, D. Yamashita, H. Seo, K. Kamataki, N. Itagaki, K. Koga, and M. Shiratani. *Journal of Physics: Conference Series*, 518(1), 2014.

[18] K. Hassouni, C. D. Scott, S. Farhat, A. Gicquel, and M. Capitelli. *Surface and Coatings Technology*, 97(1-3):391–403, 1997.

[19] Toshio Hayashi, Kenji Ishikawa, Makoto Sekine, and Masaru Hori. *Japanese Journal of Applied Physics*, 55(7S2):07LD07, jul 2016.

[20] Gregory A Hebner, Edward V Barnat, Paul A Miller, Alex M Paterson, and John P Holland. *Plasma Sources Science and Technology*, 15(4):879–888, nov 2006.

[21] Hiroshi AMEMIYA. *Journal of the Physical Society of Japan*, 81:1–7, 2012.

[22] International Renewable Energy Agency (IRENA). pages 1–96, 2018.

[23] Shin Ichiro Ishihara, Masatoshi Kitagawa, Takashi Hirao, Kiyotaka Wasa, Takashi Arita, and Koshiro Mori. *Journal of Applied Physics*, 62(2):485–491, 1987.

[24] Junghoon Joo. *Thin Solid Films*, 519(20):6892–6895, 2011.

[25] Yoshinobu Kawai, Yoshiaki Takeuchi, Hiroshi Mashima, Yasuhiro Yamauchi, and Hiromu Takatsuka. *Plasma Processes and Polymers*, 2(9):695–701, nov 2005.

[26] K. Kawamura, H. Mashima, Y. Takeuchi, A. Takano, M. Noda, Y. Yonekura, and H. Takatsuka. *Thin Solid Films*, 506-507:22–26, 2006.

[27] Kimitaka Keya, Takashi Kojima, Yoshihiro Torigoe, Susumu Toko, Daisuke Yamashita, Hyunwoong Seo, Naho Itagaki, Kazunori Koga, and Masaharu Shiratani. *Japanese Journal of Applied Physics*, 55(7S2):07LE03, jul 2016.

[28] Ho Jun Kim and Hae June Lee. *Plasma Sources Science and Technology*, 26(8):85003, 2017.

[29] Kazunori Koga, Toshihisa Inoue, Kouki Bando, Shinya Iwashita, Masaharu Shiratani, and Yukio Watanabe. *Japanese Journal of Applied Physics*, 44(No. 48):L1430–L1432, nov 2005.

[30] U. Kroll, A. Shah, H. Keppner, J. Meier, P. Torres, and D. Fischer. *Solar Energy Materials and Solar Cells*, 48(1997):343–350, 1997.

[31] Mark J. Kushner. *Journal of Applied Physics*, 63(8):2532–2551, 1988.

[32] Mark J. Kushner. *Journal of Applied Physics*, 71(9):4173–4189, 1992.

[33] M. A. Lieberman, J. P. Booth, P. Chabert, J. M. Rax, and M. M. Turner. *Plasma Sources Science and Technology*, 11(3):283–293, 2002.

[34] Michael A. Lieberman and Allan J. Lichtenberg. Capacitive discharges. In *Principles of Plasma Discharges and Materials Processing*, chapter 11. John Wiley & Sons, Inc., Hoboken, NJ, USA, apr 2005.

[35] Cheng Yang Lien, Chia Fu Chen, Ching Lung Yang, Yoshinobu Kawai, Kuo Feng Chiu, Jen Bin Shi, Sy Ruen Huang, Jui Hao Wang, Yu Jer Tsai, and Ting Kuei Lien. *Japanese Journal of Applied Physics*, 54(9):2–6, 2015.

[36] Cheng-Yang Lien, Chia-Fu Chen, Ching-Lung Yang, Yoshinobu Kawai, Kuo-Feng Chiu, Jen-Bin Shi, Jui-Hao Wang, Shui-Yang Lien, Yu-Jer Tsai, and Ting-Kuei Lien. *Vacuum*, 121:289–293, nov 2015.

[37] D.P. Lymberopoulos and D.J. Economou. *Journal of Research of the National Institute of Standards and Technology*, 100(4):473, 1995.

[38] D. Mataras. *Pure and Applied Chemistry*, 77(2):379–389, jan 2005.

[39] Akihisa Matsuda. *Japanese Journal of Applied Physics*, 43(12):7909–7920, 2004.

[40] Akihisa Matsuda, Takao Kaga, Hideo Tanaka, and Kazunobu Tanaka. *Journal of Non-Crystalline Solids*, 59-60:687–690, dec 1983.

[41] Akihisa Matsuda, Madoka Takai, Tomonori Nishimoto, and Michio Kondo. *Solar Energy Materials and Solar Cells*, 78(1-4):3–26, 2003.

[42] Takuya Matsui, Hitoshi Sai, Kimihiko Saito, and Michio Kondo. *Progress in Photovoltaics: Research and Applications*, 21(6):1363–1369, sep 2013.

[43] G. J. Nienhuis, W. J. Goedheer, E. A.G. Hamers, W. G.J.H.M. Van Sark, and J. Bezemer. *Journal of Applied Physics*, 82(5):2060–2071, 1997.

[44] Chisato Niikura, Naho Itagaki, Michio Kondo, Yoshinobu Kawai, and Akihisa Matsuda. *Thin Solid Films*, 457(1):84–89, 2004.

[45] Chisato Niikura, Naho Itagaki, and Akihisa Matsuda. *Japanese Journal of Applied Physics, Part 1: Regular Papers and Short Notes and Review Papers*, 46(5 A):3052–3058, 2007.

[46] Chisato Niikura, Michio Kondo, and Akihisa Matsuda. *Solar Energy Materials and Solar Cells*, 90(18-19):3223–3231, 2006.

[47] T. Nishimiya, Y. Takeuchi, Y. Yamauchi, H. Takatsuka, T. Shioya, H. Muta, and Y. Kawai. *Thin Solid Films*, 516(13):4430–4434, 2008.

[48] Tomonori Nishimoto, Madoka Takai, Hiroomi Miyahara, Michio Kondo, and Akihisa Matsuda. *Journal of Non-Crystalline Solids*, 299-302(PART 2):1116–1122, apr 2002.

[49] NIST. 2014, https://kinetics.nist.gov/kinetics/Detail?id=1987MAT/YUU1575-1581:2.

[50] S. Nunomura and M. Kondo. *Applied Physics Letters*, 93(23):231502, dec 2008.

[51] Kohei Ogiwara, Weiting Chen, Kiichiro Uchino, and Yoshinobu Kawai. *Japanese Journal of Applied Physics*, 52(11 PART 2):2–6, 2013.

[52] Kohei Ogiwara, Weiting Chen, Kiichiro Uchino, and Yoshinobu Kawai. *Thin Solid Films*, 547:132–136, 2013.

[53] Kohei Ogiwara, Weiting Chen, Kiichiro Uchino, and Yoshinobu Kawai. *Japanese Journal of Applied Physics*, 54(1S):01AC04, jan 2015.

[54] Yasunori Ohtsu and Yujiro Kawasaki. *Journal of Applied Physics*, 113(3):033302, jan 2013.

[55] Lawrence J. Overzet and Michael B. Hopkins. *Applied Physics Letters*, 63(18):2484–2486, nov 1993.

[56] PEGASUS Software Inc. http://www.psinc.co.jp/english/index.html.

[57] J. Perrin, O. Leroy, and M. C. Bordage. *Contributions to Plasma Physics*, 36(1):3–49, 1996.

[58] S. C. Brown. *Introduction to Electrical Discharges in Gases*. New York, 1966.

[59] Ikuo Sawada, Peter L G Ventzek, Barton Lane, Tatsuro Ohshita, Rochan R. Upadhyay, and Laxminarayan L. Raja. *Japanese Journal of Applied Physics*, 53(3S2):03DB01, jan 2014.

[60] A. V. Shah, J. Meier, E. Vallat-Sauvain, N. Wyrsch, U. Kroll, C. Droz, and U. Graf. *Solar Energy Materials and Solar Cells*, 78(1-4):469–491, 2003.

[61] Satoshi Shimizu, Michio Kondo, and Akihisa Matsuda. *Journal of Applied Physics*, 97(3):033522, feb 2005.

[62] T SHIRAFUJI, K TACHIBANA, and Y MATSUI. 1995, papers2://publication/uuid/40A8B1E4-7024-4F7C-9FC6-DD351833300C.

[63] H. Sonobe, A. Sato, S. Shimizu, T. Matsui, M. Kondo, and A. Matsuda. *Thin Solid Films*, 502(1-2):306–310, apr 2006.

[64] D. L. Staebler and C. R. Wronski. *Applied Physics Letters*, 31(4):292–294, 1977.

[65] Mikio Taguchi, Akira Terakawa, Eiji Maruyama, and Makoto Tanaka. *Progress in Photovoltaics: Research and Applications*, 13(6):481–488, sep 2005.

[66] Madoka Takai, Tomonori Nishimoto, Michio Kondo, and Akihisa Matsuda. *Applied Physics Letters*, 77(18):2828–2830, 2000.

[67] Hiromu Takatsuka, Matsuhei Noda, Yoshimichi Yonekura, Yoshiaki Takeuchi, and Yasuhiro Yamauchi. *Solar Energy*, 77(6):951–960, 2004.

[68] Yoshiaki Takeuchi, Hiroshi Mashima, Masayoshi Murata, Satoshi Uchino, and Yoshinobu Kawai. *Japanese Journal of Applied Physics*, 40(Part 1, No. 5A):3405–3408, may 2001.

[69] M. M. Turner. *Physics of Plasmas*, 13(3):033506, mar 2006.

[70] U.S. Energy Information Administration. 2016, http://www.eia.gov/beta/international/ana-lysis.php?iso=TWN.

[71] J. P. Verboncoeur. *Plasma Physics and Controlled Fusion*, 47(5 A), 2005.

[72] World Nuclear Association. 2018, http://www.world-nuclear.org/information-library/country-profiles/others/nuclear-power-in-taiwan.aspx.

[73] Tsukasa Yamane, Shinya Nakano, Sachiko Nakao, Yoshiaki Takeuchi, Ryuta Ichiki, Hiroshi Muta, Kiichiro Uchino, and Yoshinobu Kawai. *Japanese Journal of Applied Physics*, 53(11):116101, nov 2014.

[74] Y. Yamauchi, Y. Takeuchi, H. Takatsuka, H. Yamashita, H. Muta, and Y. Kawai. *Contributions to Plasma Physics*, 48(4):326–330, 2008.

[75] Yohei Yamazawa. *Applied Physics Letters*, 95(19), 2009.

[76] Yang Yang and Mark J. Kushner. *Plasma Sources Science and Technology*, 19(5), 2010.

[77] Akimasa Yuuki, Yasuji Matsui, and Kunihide Tachibana. *Japanese Journal of Applied Physics*, 28(Part 1, No. 2):212–218, feb 1989.

Appendix 1

Electron impact cross sections for SiH_4 gas. Ref. [31]

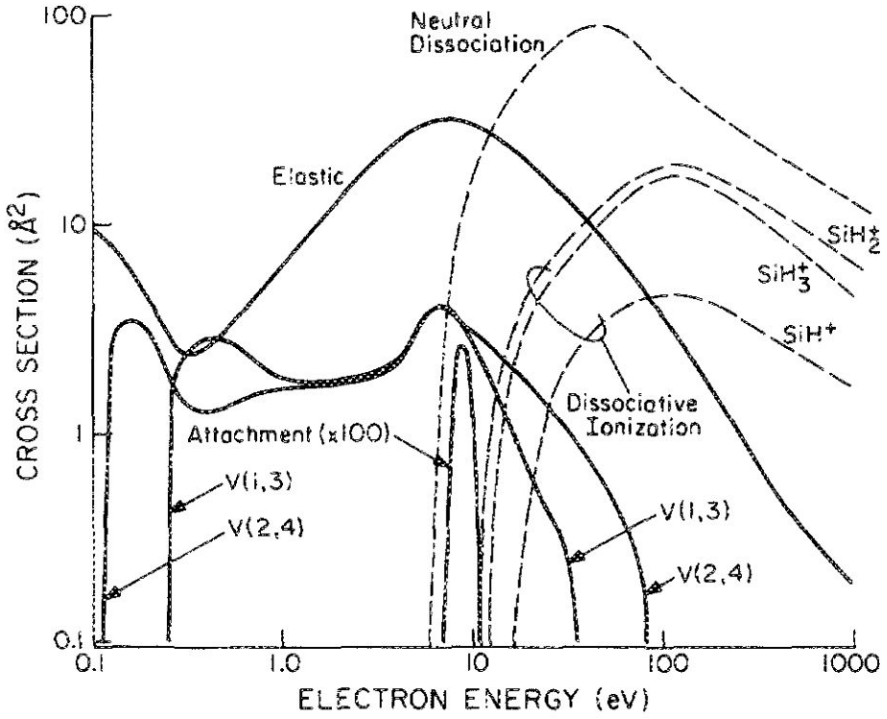

Appendix 2

Balanced power feeding schema Ref. [47]

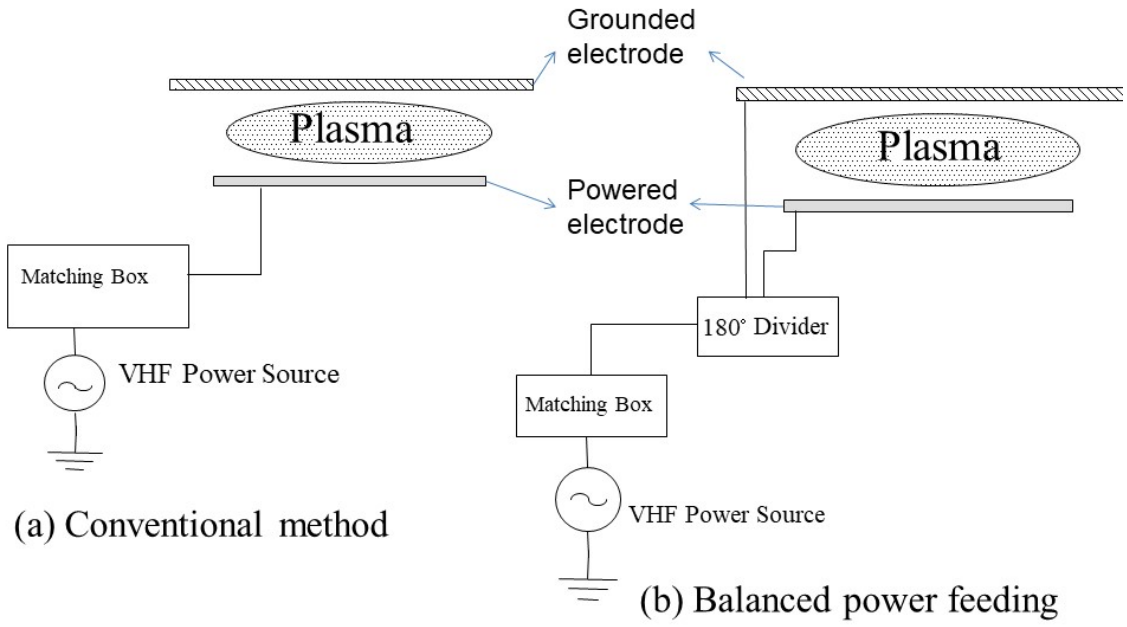

Appendix 3

Fluid equations used in Plasma Hybrid Module

Continuity equation

$$\frac{\partial n}{\partial t} + \nabla \cdot n\boldsymbol{v} = R$$

Equation of motion

$$\frac{\partial mn\boldsymbol{v}}{\partial t} + \nabla \cdot mn\boldsymbol{v}\boldsymbol{v} + \nabla \cdot \boldsymbol{P} - neZ\boldsymbol{E} = \boldsymbol{R}_{mom}$$

Energy balance equation

$$\frac{\partial n\langle\varepsilon\rangle}{\partial t} + \nabla \cdot n\boldsymbol{v}\langle\varepsilon\rangle + \nabla \cdot \boldsymbol{P} \cdot \boldsymbol{v} + \nabla \cdot \boldsymbol{Q} + en\boldsymbol{v} \cdot \boldsymbol{E} = R_{eng}$$

R: Particle production rate due to ionization and others
$\mathbf{R}_{mom}$: Exchange rate of momentum caused by collisions
R_{eng}: Exchange rate of energy caused by collisions
P: Stress tensor
Q: Heat flux vector
$\varepsilon = (1/2)m\langle v^2\rangle$

Appendix 4

Simulated silane SiH_4 plasma reactions - full overview for use with PEGASUS Software.

$$e^- + e^- \longrightarrow e^- + e^-$$

$$e^- + H \longrightarrow 2\,e^- + H^+$$

$$e^- + H^{2s} \longrightarrow e^- + H^+ + e^-$$

$$H^- + H \longrightarrow e^- + H_2$$

$$H^- + H^+ \longrightarrow 2\,H$$

$$e^- + H_2 \longrightarrow H_2 + e^-$$

$$e^- + H_2 \longrightarrow H_2{}^+ + e^- + e^-$$

$$e^- + H_2 \longrightarrow e^- + H + H^{L-alp} \longrightarrow e^- + H + H$$

$$e^- + H_2 \longrightarrow e^- + H_2{}^{L-bnd} \longrightarrow e^- + H_2$$

$$e^- + H_2 \longrightarrow e^- + H_2{}^{W-bnd} \longrightarrow e^- + H_2$$

$$e^- + H_2 \longrightarrow e^- + H + H^{2s}$$

$$e^- + H_2 \longrightarrow e^- + H_2{}^{J=0-2} \longrightarrow e^- + H_2$$

$$e^- + H_2 \longrightarrow e^- + H_2{}^{J=1-3} \longrightarrow e^- + H_2$$

$$e^- + H_2 \longrightarrow 2\,e^- + H + H^+$$

$$e^- + H_2 \longrightarrow H + H + e^-$$

$$e^- + H_2 \longrightarrow H_2{}^{v1,v2,v3} + e^- \longrightarrow H_2 + e^-$$

$$e^- + H_2 \longrightarrow e^- + H_2{}^{B^1\sigma_u} \longrightarrow e^- + H_2$$

$$e^- + H_2 \longrightarrow e^- + H_2{}^{C^1\pi_u} \longrightarrow e^- + H_2$$

$$e^- + H_2 \longrightarrow e^- + H_2{}^{b^3\sigma_u} \longrightarrow e^- + H_2$$

$$e^- + H_2 \longrightarrow H^- + H$$

$$H_2^+ + H_2 \longrightarrow H_3^+ + H$$

$$H_2^+ + H_2 \longrightarrow H^+ + H + H_2$$

$$H^- + H_2 \longrightarrow e^- + H + H_2$$

$$H_2^+ + H \longrightarrow H^+ + H_2$$

$$e^- + H_2^+ \longrightarrow 2\,H$$

$$e^- + H_2^+ \longrightarrow e^- + H^+ + H$$

$$e^- + H_2^+ \longrightarrow H^+ + H^-$$

$$e^- + H^- \longrightarrow 2\,e^- + H$$

$$H_2^+ + H^- \longrightarrow H_2 + H$$

$$H_3^+ + H^- \longrightarrow H_2 + 2\,H$$

$$e^- + H_3^+ \longrightarrow H_2 + H$$

$$e^- + H_3^+ \longrightarrow e^- + H^+ + 2\,H$$

$$e^- + H_3^+ \longrightarrow 3\,H$$

$$e^- + SiH_4 \longrightarrow SiH_4 + e^-$$

$$e^- + SiH_4 \longrightarrow SiH_3^+ + H + e^- + e^-$$

$$e^- + SiH_4 \longrightarrow SiH_3^- + H$$

$$e^- + SiH_4 \longrightarrow SiH_4^{v13} + e^- \longrightarrow SiH_4 + e^-$$

$$e^- + SiH_4 \longrightarrow SiH_4^{v24} + e^- \longrightarrow SiH_4 + e^-$$

$$e^- + SiH_4 \longrightarrow SiH^+ + H_2 + H + e^- + e^-$$

$$e^- + SiH_4 \longrightarrow SiH_3 + H + e^-$$

$$e^- + SiH_4 \longrightarrow SiH_2 + 2\,H + e^-$$

$$e^- + SiH_4 \longrightarrow SiH + 3\,H + e^-$$

$$e^- + SiH_4 \longrightarrow SiH_2^+ + 2\,H + e^- + e^-$$

$$e^- + SiH_4 \longrightarrow Si^+ + 2\,H_2 + e^- + e^-$$

$$e^- + Si_2H_6 \longrightarrow Si_2H_4^+ + 2\,H + e^- + e^-$$

$$e^- + Si_2H_6 \longrightarrow SiH_3 + SiH_2 + H + e^-$$

$$SiH_2^+ + SiH_4 \longrightarrow SiH_3^+ + SiH_3$$

$$H_3^+ + SiH_4 \longrightarrow SiH_3^+ + 2\,H_2$$

$$H_2^+ + SiH_4 \longrightarrow SiH_3^+ + H_2 + H$$

$$H^+ + SiH_4 \longrightarrow SiH_3^+ + H_2$$

$$H + SiH_4 \longrightarrow SiH_3 + H_2$$

$$H + Si_2H_6 \longrightarrow Si_2H_5 + H_2$$

$$H + Si_2H_6 \longrightarrow SiH_3 + SiH_4$$

$$H_2 + SiH_2 \longrightarrow SiH_4$$

$$SiH_4 + SiH_2 \longrightarrow Si_2H_6$$

$$Si_2H_6 + SiH_2 \longrightarrow Si_3H_8$$

$$SiH_3 + SiH_3 \longrightarrow SiH_4 + SiH_2$$

$$SiH_3^- + SiH_2^+ \longrightarrow SiH_3 + SiH_2$$

$$SiH_3^- + Si_2H_4^+ \longrightarrow SiH_3 + 2\,SiH_2$$

$$H_2^+ + SiH_3^- \longrightarrow H_2 + SiH_3$$

$$H_2^+ + SiH_4 \longrightarrow Si^+ + 3\,H_2$$

$$Si^+ + SiH_4 \longrightarrow Si_2H_2^+ + H_2$$

$$e^- + Si_2H_2^+ \longrightarrow 2\,Si + H_2$$

$$Si + H_2 \longrightarrow SiH_2$$

$$SiH_3^- + SiH_3^+ \longrightarrow 2\,SiH_3$$

$$e^- + SiH_3^+ \longrightarrow SiH_2 + H$$

$$SiH_3^- + H_3^+ \longrightarrow SiH_4 + H_2$$

$$H^+ + SiH_3^- \longrightarrow SiH_4$$

$$SiH_2 + Si_3H_8 \longrightarrow Si_4H_{10}$$

$$Si_2H_5 + Si_2H_5 \longrightarrow Si_4H_{10}$$

$$Si_2H_4 + Si_2H_6 \longrightarrow Si_4H_{10}$$

$$Si_4H_9 \longrightarrow Si_4H_{10}$$

$$SiH + Si_4H_{10} \longrightarrow Si_5H_{11}$$

$$SiH_2 + Si_4H_{10} \longrightarrow Si_5H_{12}$$

$$SiH_3 + Si_4H_{10} \longrightarrow Si_5H_{11} + H_2$$

$$SiH_3^+ + Si_4H_{10} \longrightarrow Si_5H_{10}^+ + H_2 + H$$

$$SiH_2^+ + Si_4H_{10} \longrightarrow Si_5H_{10}^+ + H_2$$

$$SiH^+ + Si_4H_{10} \longrightarrow Si_5H_{10}^+ + H$$

$$SiH_4 + Si \longrightarrow SiH_2 + SiH_2$$

$$SiH_4 + SiH \longrightarrow Si_2H_5$$

$$SiH_4 + SiH \longrightarrow Si_2H_3 + H_2$$

$$SiH_4 + SiH_3 \longrightarrow Si_2H_5 + H_2$$

$$SiH_4 + Si_2H_4 \longrightarrow Si_3H_8$$

$$SiH_4 + Si_2H_5 \longrightarrow Si_2H_6 + SiH_3$$

$$Si_2H_6 + SiH_3 \longrightarrow SiH_4 + Si_2H_5$$

$$Si_2H_6 + SiH \longrightarrow Si_3H_7$$

$$SiH_3 + H \longrightarrow SiH_2 + H_2$$

$$SiH_3 + SiH_2 \longrightarrow Si_2H_5$$

$$SiH_3 + Si_2H_5 \longrightarrow Si_3H_8$$

$$SiH_2 \longrightarrow Si_2H_2$$

$$SiH_2 + SiH \longrightarrow Si_2H_3$$

$$SiH_2 + H \longrightarrow SiH + H_2$$

$$SiH_2 \longrightarrow SiH_3$$

$$SiH + H_2 \longrightarrow SiH_3$$

$$Si_2H_4 + H_2 \longrightarrow Si_2H_6$$

$$Si_2H_4 + H_2 \longrightarrow SiH_4 + SiH_2$$

$$Si_2H_3 + H_2 \longrightarrow Si_2H_5$$

$$Si_2H_2 + H_2 \longrightarrow Si_2H_4$$

$$Si_2H_2 \longrightarrow Si_2H_3$$

$$SiH + Si_2H_6 \longrightarrow Si_3H_7$$

$$Si_3H_7 \longrightarrow Si_3H_8$$

$$SiH + Si_3H_8 \longrightarrow Si_4H_9$$

$$SiH_3 + Si_3H_8 \longrightarrow Si_4H_9 + H_2$$

$$Si_5H_{11} \longrightarrow Si_5H_{12}$$

$$SiH_3^+ + SiH_4 \longrightarrow Si_2H_3^+ + 2\,H_2$$

$$SiH_3^+ + SiH_4 \longrightarrow Si_2H_5^+ + H_2$$

$$SiH_3^+ + Si_2H_6 \longrightarrow Si_2H_5^+ + SiH_4$$

$$SiH_3^+ + Si_2H_6 \longrightarrow Si_3H_6^+ + H_2 + H$$

$$SiH_3^+ + Si_3H_8 \longrightarrow Si_4H_8^+ + H_2 + H$$

$$SiH_2^+ + SiH_4 \longrightarrow Si_2H_2^+ + 2\,H_2$$

$$SiH_2^+ + SiH_4 \longrightarrow Si_2H_4^+ + H_2$$

$$SiH_2^+ + Si_2H_6 \longrightarrow Si_2H_2^+ + SiH_4 + H_2$$

$$SiH_2^+ + Si_2H_6 \longrightarrow Si_2H_5^+ + SiH_3$$

$$SiH_2^+ + Si_2H_6 \longrightarrow Si_3H_6^+ + H_2$$

$$SiH_2^+ + Si_3H_8 \longrightarrow Si_4H_8^+ + H_2$$

$$SiH^+ + SiH_4 \longrightarrow Si_2H^+ + 2\,H_2$$

$$SiH^+ + SiH_4 \longrightarrow Si_2H_3^+ + H_2$$

$$SiH^+ + Si_2H_6 \longrightarrow Si_2H^+ + SiH_4 + H_2$$

$$SiH^+ + Si_2H_6 \longrightarrow Si_2H_3^+ + SiH_4$$

$$SiH^+ + Si_2H_6 \longrightarrow Si_3H_6^+ + H$$

$$SiH^+ + Si_3H_8 \longrightarrow Si_4H_8^+ + H$$

$$Si^+ + Si_2H_6 \longrightarrow Si_2H_2^+ + SiH_4$$

$$Si^+ + Si_2H_6 \longrightarrow Si_3H_6^+$$

$$Si_2H_5^+ + SiH_4 \longrightarrow Si_3H_6^+ + H_2 + H$$

$$Si_2H_4^+ + SiH_4 \longrightarrow Si_3H_6^+ + H_2$$

$$Si_2H_3^+ + SiH_4 \longrightarrow Si_3H_6^+ + H$$

$$Si_2H_2^+ + SiH_4 \longrightarrow Si_3H_6^+$$

$$Si_2H_2^+ + SiH_4 \longrightarrow Si_3H_4^+ + H_2$$

$$Si_2H^+ + SiH_4 \longrightarrow Si_2H_2^+ + 2\,H_2$$

$$Si_2H_5^+ + Si_2H_6 \longrightarrow Si_3H_6^+ + SiH_4 + H$$

$$Si_2H_4^+ + Si_2H_6 \longrightarrow Si_3H_6^+ + SiH_4$$

$$Si_2H_4^+ + Si_2H_6 \longrightarrow Si_4H_8^+ + H_2$$

$$Si_2H_3^+ + Si_2H_6 \longrightarrow Si_3H_6^+ + SiH_3$$

$$Si_2H_3^+ + Si_2H_6 \longrightarrow Si_4H_8^+ + H$$

$$Si_2H_2^+ + Si_2H_6 \longrightarrow Si_3H_6^+ + SiH_2$$

$$Si_2H_2^+ + Si_2H_6 \longrightarrow Si_4H_8^+$$

$$Si_2H^+ + Si_2H_6 \longrightarrow Si_3H_6^+ + SiH$$

$$Si_2H^+ + Si_2H_6 \longrightarrow Si_4H_8^+$$

$$Si_3H_4^+ + SiH_4 \longrightarrow Si_4H_6^+ + H_2$$

$$Si_4H_6^+ + SiH_4 \longrightarrow Si_5H_{10}^+$$

$$H_2^+ + SiH_4 \longrightarrow SiH^+ + 2\,H_2 + H$$

$$H_2^+ + SiH_4 \longrightarrow SiH_2^+ + 2\,H_2$$

$$H_2^+ + SiH_4 \longrightarrow SiH_3 + H_3^+$$

$$e^- + SiH^+ \longrightarrow Si + H$$

$$e^- + Si_2H^+ \longrightarrow Si + 2\,H$$

$$e^- + Si_3H_6^+ \longrightarrow Si_2H_4 + SiH_2$$

$$e^- + Si_4H_8^+ \longrightarrow Si_2H_6 + Si_2H_2$$

$$e^- + Si_5H_{10}^+ \longrightarrow Si_3H_8 + Si_2H_2$$

$$e^- + SiH_2^+ \longrightarrow SiH + H$$

$$SiH_2^+ + H_2 \longrightarrow SiH_3^+ + H$$

$$e^- + Si \longrightarrow Si^+ + 2\,e^-$$